# Extreme Precipitation Events in Northern California during Winter 2016–17: Multiscale Analysis and Climatological Perspective

BENJAMIN J. MOORE, ALLEN B. WHITE, DANIEL J. GOTTAS, AND PAUL J. NEIMAN

*NOAA/Earth System Research Laboratory, Physical Sciences Division, Boulder, Colorado*

(Manuscript received 19 July 2019, in final form 27 November 2019)

ABSTRACT

A multiscale analysis is presented of extreme precipitation events (EPEs) in Northern California during winter 2016–17, which caused flooding and contributed substantially to highly anomalous seasonal precipitation totals. The EPEs were characterized by long durations (≥7 days) and involved persistent large-scale flow patterns. The three largest EPEs involved blocking over the Bering Sea–Alaska region. A detailed investigation of the largest EPE, occurring on 2–10 February 2017, reveals that extreme precipitation was produced as four discrete cyclones moved across the eastern North Pacific equatorward of a high-amplitude blocking ridge and impacted the U.S. West Coast in rapid succession. The latter three cyclones developed and moved in conjunction with elongated negatively tilted troughs or PV streamers resulting from repeated episodes of baroclinic development and cyclonic Rossby wave breaking on the upstream flank of the block. Each of the four cyclones interacted with a PV streamer and an associated baroclinic zone established by anticyclonic wave breaking on the downstream flank of the block and, thereby, tracked into the U.S. West Coast. The serial clustering of the cyclones during the 9-day event resulted in persistent water vapor flux and lifting that supported extreme precipitation totals in Northern California. A climatological analysis for 1979–2017 reveals a significant statistical relationship between blocking over the Bering Sea–Alaska region and EPEs in Northern California, indicating that this type of blocking pattern represents a favorable large-scale scenario for extreme precipitation in Northern California.

## 1. Introduction

### *a. Motivation and objectives*

In winter 2016–17, California experienced a series of extreme precipitation events (EPEs) that resulted in hazardous flooding and contributed substantially to extraordinary seasonal precipitation accumulations (NOAA/NWS/CNRFC 2018; NOAA/NCEI 2018; White et al. 2019). The precipitation totals over California departed markedly from the long-term climatology during the winter (Fig. 1a) and were largest and most anomalous in Northern California, particularly the northern Sierra Nevada (Figs. 1b–d). Precipitation accumulations during December–February were often concentrated in large steps (Fig. 1a), suggestive of contributions from individual EPEs. These events generally comprised prolonged periods (e.g., ≥7 days) of moderate and heavy precipitation that resulted in large runoff and flooding (NOAA/NWS/CNRFC 2018; White et al. 2019). One such EPE during 2–10 February 2017 over the northern Sierra Nevada led to significant flooding and nearly caused a serious disaster at the Oroville Dam (White et al. 2019). Despite their deleterious impacts, the EPEs provided crucial water resources to California and helped to ameliorate and, at many locations, bring an end to severe drought conditions (e.g., NOAA/NCEI 2018; Wang et al. 2017).

The significant hydrological impacts in California during winter 2016–17 motivate a systematic analysis of the processes governing the aforementioned EPEs. Such an analysis may help to advance the overall physical understanding of EPEs in California. Herein, a multiscale diagnostic investigation of the events in winter 2016–17 is conducted, with a specific focus on Northern California. The objectives of this investigation are: 1) to identify recurrent large-scale flow patterns that resulted in the EPEs during the winter, and 2) to diagnose processes that acted to sustain precipitation over Northern California during the events. In addition, a

*Corresponding author*: Dr. Benjamin J. Moore, benjamin.moore@noaa.gov

DOI: 10.1175/MWR-D-19-0242.1

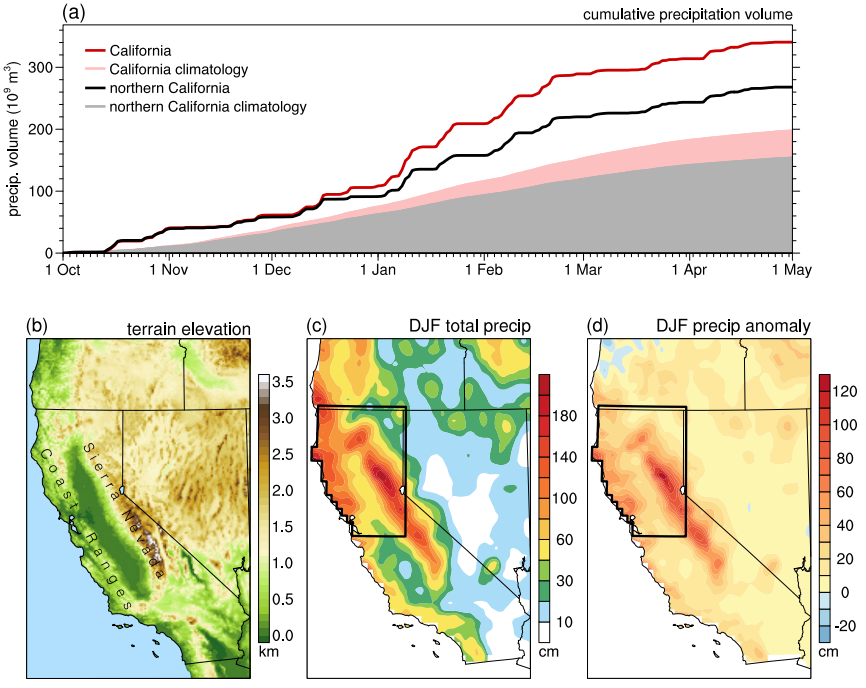


FIG. 1. (a) Time series of the cumulative precipitation volume for all of California (red curve) and for Northern California (black curve) for October 2016–April 2017 with corresponding 1979–2015 climatological mean time series shown in the pink and gray, respectively. Maps of (b) 1-arc-min terrain elevation (shaded in km), (c) December 2016–February 2017 total precipitation (shaded in cm), and (d) December 2016–February 2017 total precipitation anomaly relative to the 1979–2015 climatology (shaded in cm). The domain for the Northern California time series in (a) is outlined in black in (c),(d). Precipitation data are from the 0.25° NOAA Climate Prediction Center Unified Precipitation Dataset.

complementary climatological perspective on EPEs in Northern California is provided.

### b. *Literature review*

In California, EPEs predominantly occur during the cool season in connection with baroclinic waves and associated extratropical cyclones (e.g., Maddox et al. 1980; Junker et al. 2008; Dettinger et al. 2011; Pfahl and Wernli 2012; Ralph and Dettinger 2012). These events tend to feature strong, sustained water vapor flux within long, narrow corridors, referred to as atmospheric rivers (ARs; e.g., Newell et al. 1992; Zhu and Newell 1998; Ralph et al. 2004, 2005, 2006, 2018; Neiman et al. 2008; Cordeira et al. 2013), that are aligned with the precold-frontal low-level jet (e.g., Browning and Pardoe 1973) in the warm sector of a cyclone.[1] Heavy precipitation is often produced through orographic lifting in the presence of moist-neutral stratification as the water vapor flux impinges upon elevated terrain (see Fig. 1b) in California (e.g., Neiman et al. 2002; Smith et al. 2010). Dynamically forced lifting along baroclinic zones and fronts associated with a cyclone may also contribute to the generation of precipitation (e.g., Browning 1986; Hecht and Cordeira 2017). This lifting may be manifested by coherent ascending airstreams extending through the cyclone warm sector referred to as warm conveyor belts (e.g., Harrold 1973; Carlson 1980; Wernli 1997; Madonna et al. 2014; Pfahl et al. 2014). Extreme precipitation can result when the ingredients sustaining precipitation—water vapor supply and lifting—are forced to persist over a given location for a long duration [e.g., multiple days (e.g., Doswell et al. 1996; Ralph et al. 2013)].

Extreme precipitation in California tends to result in configurations of the midlatitude tropopause-level jet stream over the North Pacific that support baroclinic wave activity and cyclone development in the vicinity of the U.S. West Coast. The jet stream coincides with a narrow band of enhanced potential vorticity (PV) gradients that serves as a waveguide (e.g., Martius et al. 2010) for baroclinic Rossby wave packets [see Wirth et al. (2018) and references therein] and, thereby,

[1] Further information on ARs can be found in the AMS Glossary of Meteorology (http://glossary.ametsoc.org/wiki/Atmospheric_river).

corresponds to the extratropical storm track (e.g., Chang et al. 2002). Large-scale flow patterns linked to EPEs often feature a strong and zonally elongated jet stretching over the eastern North Pacific toward the U.S. West Coast (e.g., Mo and Higgins 1998; Higgins et al. 2000a; Neiman et al. 2008; Payne and Magnusdottir 2014). In some EPE scenarios (e.g., Weaver 1962; Carrera et al. 2004; Ralph et al. 2011), the jet is subject to significant distortion and meridional displacement within persistent large-scale high-amplitude Rossby wave patterns, including those manifested in atmospheric blocking [see Woollings et al. (2018) and references therein]. Such patterns over the North Pacific may form and amplify through baroclinic processes (e.g., Dole and Black 1990; Röthlisberger et al. 2018) and diabatic processes (i.e., latent heat release) along ascending airstreams (e.g., Pfahl et al. 2015; Grams and Archambault 2016) associated with synoptic-scale disturbances. The occurrence of a blocking ridge over the central and eastern North Pacific can promote downstream trough amplification and cyclone development in the vicinity of the California coast (Weaver 1962). When blocking occurs at high latitudes over the Bering Sea and eastern Alaska, an anomalous storm track extending into California can be established on the equatorward flank of the block (Weaver 1962; Carrera et al. 2004).

Life cycles of baroclinic waves tend to culminate in a process of Rossby wave breaking (Thorncroft et al. 1993), defined as a rapid and irreversible deformation of material (i.e., PV) contours (McIntyre and Palmer 1983, 1984). Wave breaking can significantly influence the structure, evolution, and precipitation impacts of landfalling cyclones and ARs along the U.S. West Coast (e.g., Ryoo et al. 2013; Payne and Magnusdottir 2014, 2016; Hu et al. 2017). Pronounced distortions of the upper-level PV field during wave breaking typically result in the formation of elongated troughs, or PV streamers (e.g., Appenzeller and Davies 1992; Martius et al. 2007). Rossby wave breaking may occur cyclonically or anticyclonically, depending on the configuration of the background flow. Cyclonic wave breaking is characterized by a cyclonic distortion of the PV, often in conjunction with surface cyclogenesis, resulting in the formation of a negatively tilted PV streamer. Conversely, anticyclonic wave breaking is characterized by an anticyclonic distortion of the PV, resulting in the formation of a positively tilted streamer. Deformation of waves in large-scale diffluent and confluent flow fields established on the upstream and downstream flanks of a block is conducive to cyclonic and anticyclonic wave breaking, respectively (e.g., Shutts 1983; Spensberger and Spengler 2014).

Convection in the tropics can significantly affect the structure and evolution of the midlatitude jet stream over the North Pacific and thereby modulate baroclinic wave activity linked to precipitation in California. Latent heating and associated upper-level divergent outflow in an area of convection may modify the flow and generate an anomalous upper-level anticyclone (i.e., negative PV anomaly) on the equatorward side of the jet (e.g., Barlow et al. 2007). The anticyclone is linked to strengthened PV gradients and wind speeds along the jet and, by thermal wind balance, enhanced tropospheric baroclinicity below the jet core (e.g., Moore et al. 2010). Additionally, perturbation of the jet by the outflow can result in an extratropical barotropic Rossby wave response downstream (e.g., Sardeshmukh and Hoskins 1988). Anomalous convection over the central and eastern tropical Pacific linked to the El Niño–Southern Oscillation (ENSO) or the Madden–Julian oscillation (MJO) favors a strengthened and zonally extended jet stream over the central and eastern North Pacific (e.g., Knutson and Weickmann 1987; Rasmusson and Mo 1993; Higgins and Mo 1997; Shapiro et al. 2001; Winters et al. 2019). Anomalous convection centered over the Indian Ocean and the Maritime Continent region linked to La Niña conditions or the MJO favors a comparatively weak jet and the formation of high-amplitude Rossby wave patterns and blocking over the central and eastern North Pacific (e.g., Renwick and Wallace 1996; Carrera et al. 2004; Moore et al. 2010).

A distinctive aspect of the EPEs in winter 2016–17 was the long duration of precipitation in each event, corresponding to a time scale beyond that of an individual synoptic-scale baroclinic wave. Precursory analyses (NOAA/NWS/CNRFC 2018; White et al. 2019; Fish et al. 2019) indicate that the ingredients for precipitation persisted during the events in conjunction with a serial clustering of discrete cyclones along the U.S. West Coast. This clustering process is consistent with the classic concept of cyclone families (Bjerknes and Solberg 1922) and the related concept of AR families (Fish et al. 2019). Prior studies (e.g., Ralph et al. 2011; Neiman et al. 2016) have documented a similar process in which propagation of successive mesoscale waves along a cold front causes a temporary prolongation of AR conditions and precipitation along the U.S. West Coast for ~1–2 days, resulting in extreme precipitation. However, to our knowledge, EPE scenarios in this region exhibiting serial clustering of cyclones over the course of several days or more have not yet been explicitly investigated. Studies for other midlatitude regions have demonstrated that this clustering process tends to occur in conjunction with Rossby

wave breaking in persistent large-scale flow patterns characterized by zonally extended jet streams/waveguides (e.g., Sodemann and Stohl 2013; Pinto et al. 2014; Priestley et al. 2017a,b) or blocking (Grams et al. 2014). Serial clustering of such flow patterns can, analogously, result in precipitation extremes on subseasonal time scales (e.g., Martius et al. 2013; Barton et al. 2016; Lenggenhager et al. 2019).

## 2. Data and methods

### a. Datasets

Atmospheric analyses were obtained from the ECMWF interim reanalysis (ERA-Interim) dataset (ECMWF 2009; Dee et al. 2011) at 6-h intervals on a T255 (~0.7°) grid. NOAA daily mean 2.5° outgoing longwave radiation (OLR) data (Liebmann and Smith 1996; NOAA/OAR/ESRL/PSD 2019b) were used to assess large-scale cloudiness and convection. The filtering technique of Wheeler and Weickmann (2001) was applied to extract OLR anomalies associated with the MJO. Anomalies in the ERA-Interim and OLR data were calculated relative to daily climatological means for 1979–2015 that were smoothed by retaining only the first four harmonics of the annual cycle via a Fourier analysis. Mesoscale conditions were examined using 0-h analyses from the operational 3-km NOAA High-Resolution Rapid Refresh (HRRR) model (Benjamin et al. 2016) obtained from an archive at the University of Utah (Blaylock and Horel 2015; Blaylock et al. 2017).

Precipitation analyses were obtained from the 0.25° NOAA Climate Prediction Center Unified Precipitation Dataset (UPD; Higgins et al. 2000b; NOAA/NCEP/CPC 2018) and the 4-km NCEP Stage-IV dataset (Lin 2011). These datasets cover the conterminous United States and start in 1948 and 2002, respectively. Hourly precipitation gauge data at Angwin (ANG) and Four Trees (FOR) in Northern California were obtained from the California Department of Water Resources—California Data Exchange Center (CADWR 2019). Hourly averaged profiles of the horizontal wind were obtained from a 449-MHz wind profiler on the coast at Bodega Bay (BBY) and a 915-MHz wind profiler in the Central Valley at Chico (CCO). The wind profiles were combined with collocated vertically integrated water vapor (IWV) observations from dual-channel global positioning system receivers to calculate bulk upslope IWV fluxes (i.e., the product of the local upslope wind component and the IWV) and upslope flux–precipitation correlations, as in Neiman et al. (2002). Due to unavailability of IWV data at CCO, fluxes at CCO were calculated using IWV data at nearby Oroville, California. The locations of these sites will be shown later in Fig. 13. The profiler and IWV data were obtained from a NOAA/Earth System Research Laboratory Physical Sciences Division archive (NOAA/OAR/ESRL/PSD 2018).

### b. Tools and diagnostics

Analyses of PV on isentropic surfaces intersecting the dynamic tropopause (defined as the 2-PVU surface; 1 PVU = $10^{-6}\,\mathrm{K\,kg^{-1}\,m^2\,s^{-1}}$) are shown to depict the evolution of the upper-level flow and tropopause-level jet streams or waveguides. Analogous analyses of potential temperature ($\theta$) on the dynamic tropopause are also shown. During winter 2016–17, discrete polar and subtropical jet streams were frequently evident over the North Pacific and were consistently maximized at the intersection of the dynamic tropopause with the 310 and 330-K isentropic surfaces, respectively (not shown). The two jets are hereinafter graphically delineated by the 2-PVU contour on these surfaces, respectively. This multijet perspective enables diagnosis of interactions between the jets (e.g., Shapiro et al. 1999; Martius et al. 2010)

The horizontal component of the phase-independent wave activity flux of Takaya and Nakamura [2001; their Eq. (38)] was computed to diagnose synoptic-scale Rossby wave propagation on instantaneous maps. Wave packets can be visually identified and tracked as coherent corridors of this flux (Wolf and Wirth 2017). Divergence and convergence of the flux indicate sources and sinks of wave activity, respectively. The wave activity flux was computed every 6 h on isobaric surfaces following the method of Wolf and Wirth (2017, their section 2e).

Synoptic-scale Rossby wave breaking was detected as the occurrence of objectively identified PV streamers on dynamic tropopause-intersecting isentropic surfaces. Occurrences of other key flow features, including extratropical cyclones, atmospheric blocks, and warm conveyor belts, were determined using objective climatologies constructed by Sprenger et al. (2017). The flow feature data were analyzed in the form of 6-h 1° binary fields in which a value of 1 indicates that a feature occurred at given location. The identification methods and references for the streamers, cyclones, blocks, and warm conveyor belts are provided in Table 1. The reader is referred to the references for full details on the methods.

The degree of baroclinic instability was measured in terms of the Eady growth rate maximum (Lindzen and Farrell 1980):

$$\sigma_E = 0.31 f \left| \frac{\partial v}{\partial z} \right| N^{-1}, \qquad (1)$$

TABLE 1. Methods and references for the objectively identified flow features analyzed throughout the study. The extratropical cyclone, block, and warm conveyor belt data were generated by Sprenger et al. (2017).

| Feature | Method | Reference(s) |
|---|---|---|
| PV streamers | Long, narrow regions of high PV (>2 PVU) delimited by a segment of the 2-PVU contour whose endpoints are separated by a great-circle distance of <1000 km and by an along-contour distance of >3000 km. Streamers are categorized based on tilt relative to a zonal baseline. Streamers with a positive tilt (≤75°) indicate anticyclonic wave breaking, whereas those with a negative tilt (≥105°) indicate cyclonic wave breaking. | Wernli and Sprenger (2007), Moore et al. (2019) |
| Extratropical cyclones | Regions delimited by a closed sea level pressure contour surrounding a local sea level pressure minimum. | Wernli and Schwierz (2006) |
| Blocks | Contiguous regions of 500–150-hPa vertically averaged PV anomaly values of ≤ −1.3 PVU that persist for at least 5 days. Persistence is determined through a tracking procedure that requires spatial overlap of ≥70% between consecutive 6-h times. | Schwierz et al. (2004), Croci-Maspoli et al. (2007) |
| Warm conveyor belts | 48-h forward trajectories starting in the lower troposphere that ascend ≥600 hPa in the vicinity of an extratropical cyclone. Trajectory segments located in the upper troposphere (<400 hPa) are defined as warm conveyor belt outflows. | Madonna et al. (2014) |

where $f$ is the Coriolis parameter, $v$ is the horizontal wind, $z$ is the vertical height coordinate, and $N$ is the Brunt–Väisälä frequency [$N^2 = g\ \theta^{-1}(\partial\theta/\partial z)$, where $g$ is the acceleration due to gravity]. This quantity indicates the growth rate of the most unstable mode in the Eady baroclinic instability model (Eady 1949). Equation (1) was evaluated at 700 hPa following the method of Wernli et al. (2010, their section 2b).

The **Q**-vector form of the quasigeostrophic $\omega$ equation (Hoskins et al. 1978) was solved in order to distinguish synoptic-scale dynamically forced vertical motions associated with baroclinic disturbances. The equation was solved on an $f$ plane using a standard successive overrelaxation routine (Press et al. 2007, section 20.5.1) with $\omega$ set to zero at all boundaries. As in Martin (2006), the Coriolis parameter for 45.5°N and a domain-averaged static stability were used in the calculations. The resulting vertical motion is referred to as $\omega_{QG}$.

## 3. Overview of winter 2016–17

Figure 2 depicts the evolution for winter 2016–17 of the Northern Hemispheric extratropical flow and of the precipitation and vertically integrated water vapor transport (IVT) in Northern California.[2] A striking aspect of the flow evolution (Fig. 2a) is a repeated occurrence of blocking patterns over the North Pacific characterized by persistent (i.e., >10 days) large positive 300-hPa geopotential height anomalies between ~140°E and ~140°W and centered at ~170°W. These patterns appeared four times throughout the winter, with the first three instances, in mid-December, early January, and early February, respectively, each corresponding to a long-duration EPE in Northern California. The EPEs comprised prolonged (≥7 days) moderate and heavy precipitation supported by anomalously strong IVT, and corresponded to maxima in the 7-day accumulated precipitation volume exceeding the climatological 99th percentile (Figs. 2b,c). The EPE-related blocking patterns (Figs. 3a,b,d) each featured a high-amplitude Ω-shaped upper-level ridge across eastern Russia, the central North Pacific, and Alaska, flanked downstream by a trough associated with anomalous IVT directed into California. The blocking ridge axes were located over the Bering Sea and western Alaska; hence, for convenience this type of pattern is hereinafter referred to as "Bering Sea–Alaska blocking." These patterns resemble that documented by Carrera et al. (2004, see their Fig. 2) for blocking over Alaska. EPEs also occurred in the latter part of January and February, respectively. These two events produced lower precipitation totals than the other three (Fig. 2b) and involved patterns characterized by a persistent negatively tilted trough over the Gulf of Alaska (Figs. 3c,e). Each of the five EPEs involved impacts of multiple discrete cyclones (not shown), as manifested by successive peaks in the IVT anomaly time series (Fig. 2c).

Collectively the respective 7-day precipitation maxima corresponding to the five EPEs accounted for ~85%

[2] The IVT hereinafter was computed for the 1000–300-hPa layer using the method of Neiman et al. (2008).

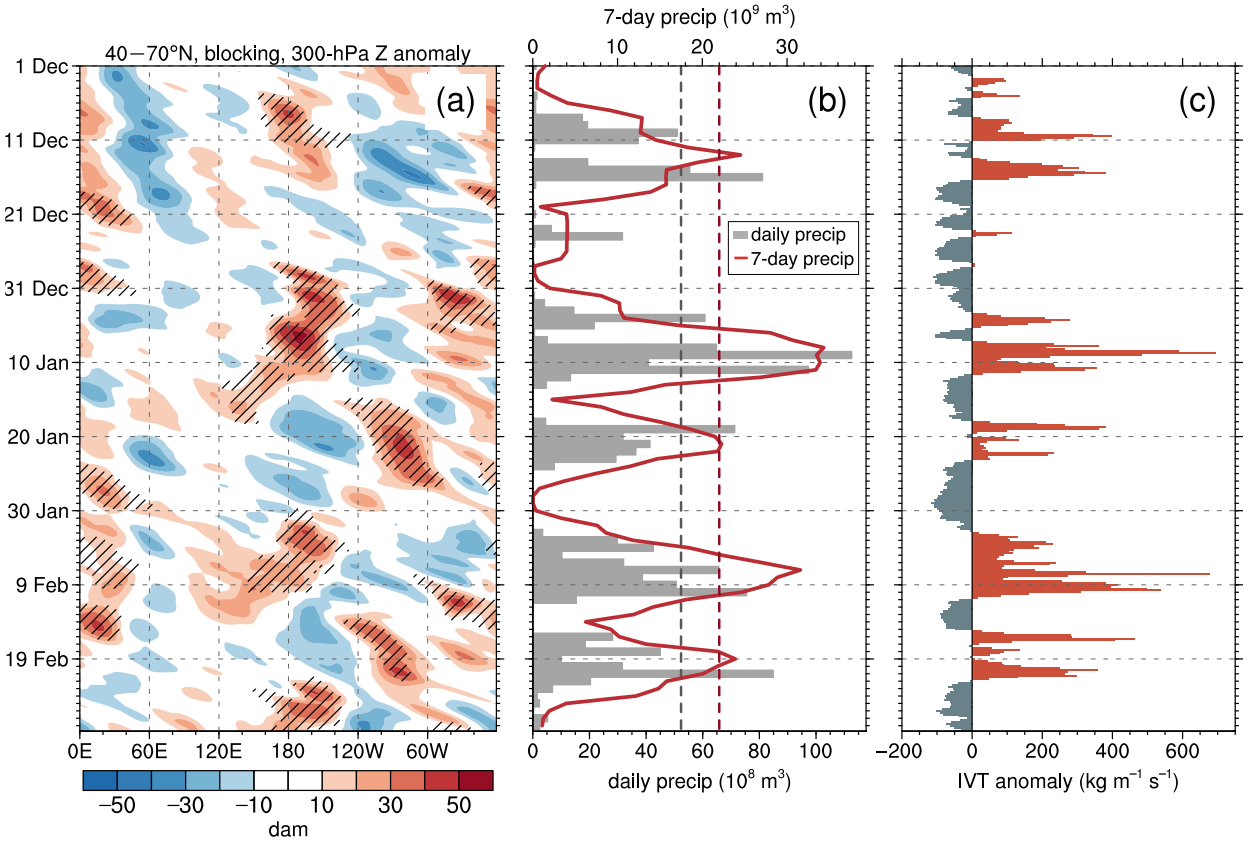


FIG. 2. (a) Hovmöller diagram showing blocking occurrences (hatching) and averaged daily mean 300-hPa geopotential height anomalies (shaded in dam) in the 40°–70°N band for 1 Dec 2016–28 Feb 2017. (b) Time series for 1 Dec 2016–28 Feb 2017 of the daily accumulated precipitation volume (gray bars) and the running 7-day accumulated precipitation volume (red curve) from the UPD for the Northern California domain depicted in Fig. 1c. The 7-day values are plotted on the center day of the corresponding 7-day period. The 99th percentile values of the daily and 7-day precipitation volume for the 1979–2017 climatology are indicated by the vertical dashed gray and red lines, respectively. (c) As in (b), but for area-averaged 6-h IVT magnitude anomalies.

of the total winter precipitation volume in Northern California. The totals for the three blocking-related EPEs together accounted for ~56%. These large precipitation contributions underscore the importance of the EPEs, particularly those related to blocking, for the anomalous winter precipitation.

During December 2016–February 2017, weak La Niña conditions [multivariate ENSO index, version 2 (Wolter and Timlin 2011; NOAA/OAR/ESRL/PSD 2019a), value of −0.41] were in place across the tropical Pacific, corresponding to a persistent envelope of negative OLR anomalies, signifying enhanced convection, centered over the Maritime Continent (Fig. 4). Tropical convective activity associated with the MJO is also evident (Fig. 4). The MJO attained a high amplitude [i.e., Real-time Multivariate MJO index (Wheeler and Hendon 2004; BOM 2019) value of >2] over the Indian Ocean (phase 2) during the late January EPE, over the Maritime Continent and the western Pacific (phases 5, 6) during the early February EPE, and over Africa (phase 8) during the late February EPE. The convection tied to La Niña conditions and the MJO potentially served as a source for extratropical Rossby wave responses that contributed to the EPEs throughout the winter, as suggested by Dong et al. (2018). Relative to prior winters during 1979–2015 that exhibited a cold ENSO phase (i.e., multivariate ENSO index value of $< -0.4$), blocking frequencies were substantially higher over the central and eastern North Pacific and coincided with a westward-shifted and amplified ridge (Figs. 5a,b). This ridge occurred as part of an amplified planetary-scale wave pattern extending across Eurasia into the North Pacific from an anomalous blocking ridge over northern Europe (Figs. 5a,b).

The results in Figs. 2, 3 suggest a dynamical role for Bering Sea–Alaska blocking in the occurrence of the Northern California EPEs during winter 2016–17.

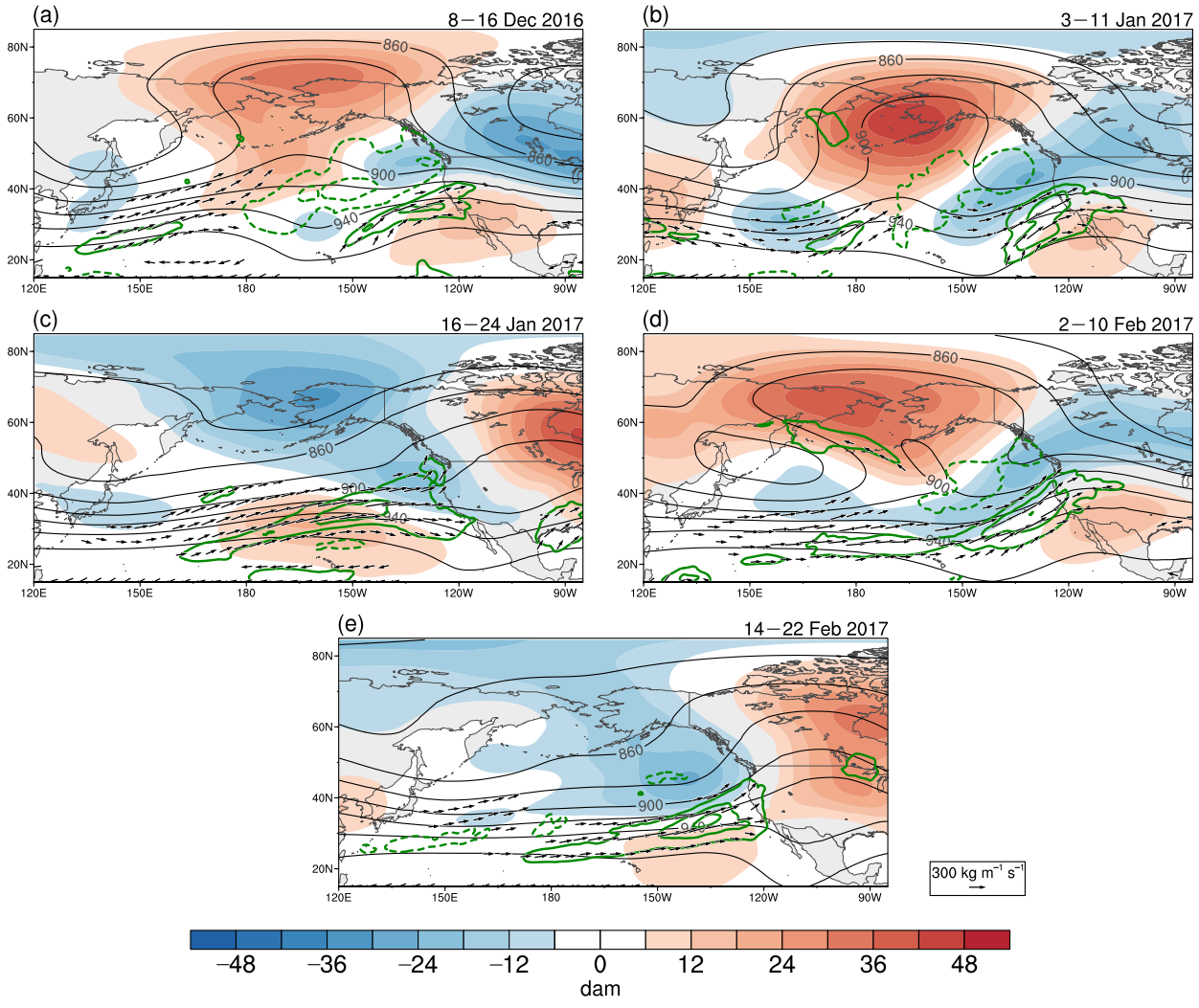


FIG. 3. Time-mean analyses for 9-day periods encompassing the five EPEs during winter 2016–17. (a) 8–16 Dec 2016, (b) 3–11 Jan 2017, (c) 16–24 Jan 2017, (d) 2–10 Feb 2017, and (e) 14–22 Feb 2017. Analyses show 300-hPa geopotential height (black, every 20 dam), 300-hPa geopotential height anomalies (shaded in dam), IVT (vectors for magnitudes ≥200 kg m$^{-1}$ s$^{-1}$, reference vector in lower right), and IVT magnitude anomalies (green contours every 100 kg m$^{-1}$ s$^{-1}$, dashed for negative values).

Prior studies (e.g., Weaver 1962; Carrera et al. 2004; Underwood et al. 2009; Hatchett et al. 2017; Fish et al. 2019) have documented a link between this type of blocking pattern and heavy or extreme precipitation in California; however, to our knowledge, dynamical processes characterizing this link have not previously been investigated in detail. Motivated by this gap in research, we present a diagnostic investigation of the early February event. Selection of this event is motivated by its significant hydrological impacts and by a desire to build upon the findings of White et al. (2019). The salient large-scale processes for this event were found to be qualitatively similar to those for the other two blocking-related EPEs (not shown).

## 4. Analysis of the early February 2017 event

### a. *Large-scale conditions*

Conditions for 1–10 February 2017 are summarized in Fig. 6. During this period, a high-amplitude blocking ridge, marked by expansive positive dynamic tropopause $\theta$ anomalies, was in place across far eastern Russia, the Bering Sea, and Alaska (Fig. 6a). As is common in blocking situations (e.g., Altenhoff et al. 2008), the block was flanked upstream by a negatively tilted trough collocated with cyclonic wave breaking activity and downstream by a positively tilted trough collocated with anticyclonic wave breaking activity along the polar jet (Fig. 6a). A single strong (>70 m s$^{-1}$) jet stream was established

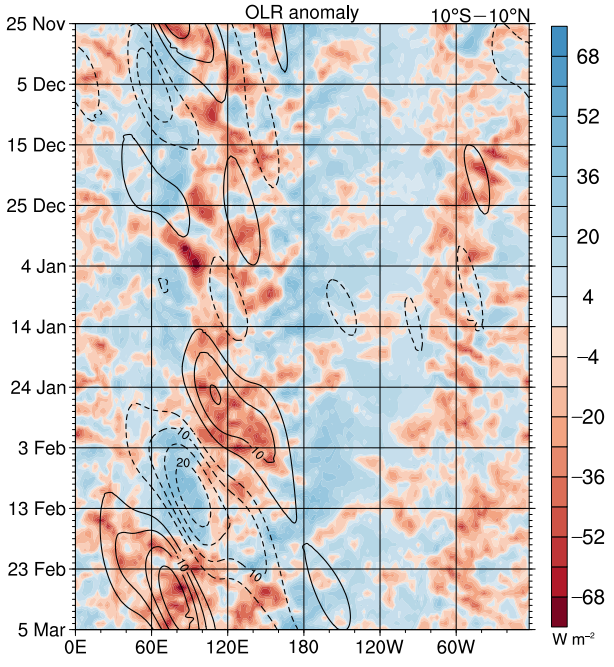


FIG. 4. Hovmöller diagram of unfiltered OLR anomalies (shaded in W m$^{-2}$) and MJO-filtered OLR anomalies (black contours every 5 W m$^{-2}$, dashed for positive values) averaged in the 10°S–10°N band for 25 Nov 2016–5 Mar 2017.

across the eastern Asia coast and the western North Pacific (~120°E–180°) upstream of the block in association with a merger of the polar and subtropical jets (Fig. 6a). The two jets exhibited a large meridional separation downstream in the blocking region. An enhanced PV gradient along the merged jet is implied on the poleward flank of a band of positive dynamic tropopause $\theta$ anomalies (i.e., negative PV anomalies). These anomalies were maintained in connection with upper-level divergent outflow, represented by the 250-hPa irrotational wind (Fig. 6b), from an expansive area of enhanced tropical convection related to the MJO (see Fig. 4) over the Maritime Continent and western tropical Pacific (~100°–160°E).[3] The outflow associated with the MJO may have additionally induced a downstream barotropic Rossby wave response supporting of the formation of the blocking pattern.

The jet merger over the western North Pacific corresponded to increased upper- and middle-tropospheric baroclinicity (not shown). Baroclinic development, as manifested by high frequencies of extratropical cyclones (Fig. 6c) and cyclonic wave breaking (Fig. 6a), occurred throughout the time period on the southwestern flank of the block (~150°E–170°W) on the cyclonic shear side and in the poleward exit region of the merged jet. The upper-level wave activity flux (Fig. 6d) indicates southeastward propagation of synoptic-scale waves along the polar jet into this development region through a corridor extending across Eurasia from a high-amplitude ridge far upstream over northern Europe (Fig. 6a). Ridge amplification during the baroclinic development episodes over the western North Pacific supported the formation and maintenance of the block, consistent with findings of prior blocking studies (e.g., Colucci 1985; Mullen 1987; Dole and Black 1990; Nakamura and Wallace 1993). Warm conveyor belts associated with western North Pacific cyclones predominantly ascended into the upper troposphere in the southwestern portion of the block (~150°E–150°W; Fig. 6c) and were associated with negative OLR anomalies and upper-level divergent outflow (Fig. 6b). Modification of the upper-level PV due to latent heat release (not shown) and resultant upper-level outflow associated with these ascending airstreams likely contributed to growth and maintenance of the block (e.g., Pfahl et al. 2015).

Wave activity flux (Fig. 6d) divergence, indicating a Rossby wave source, occurred between ~160°E and 140°W on the upstream flank of the block in the vicinity of the cyclone activity and cyclonic wave breaking. This divergence was plausibly related to eddy PV fluxes and latent heating associated with baroclinic development. The wave activity flux was directed poleward and eastward from the wave source, and, as found in prior blocking studies (e.g., Nakamura and Wallace 1990), two main corridors of wave propagation were established on the poleward and equatorward flanks of the block in approximate alignment with the polar and subtropical jets, respectively (Fig. 6d). Wave activity flux convergence occurred in western and central portions of the block (Fig. 6d) indicating absorption of wave activity.

Wave activity flux was directed southeastward through the positively tilted trough (Fig. 6d) linked to anticyclonic wave breaking on the downstream flank of the block (~120°–150°W; Fig. 6a). A strong divergence–convergence dipole occurred along the flux directed through the trough (Fig. 6d), indicating a downstream transfer of wave activity from the ridge in association with wave breaking. Confluence of the polar and subtropical jets and the corresponding wave activity fluxes is evident between 140° and 110°W in the vicinity of the positively tilted trough (Fig. 6d). This configuration suggests a potential for phasing and

[3] The irrotational wind component was computed via spherical harmonics using the NCAR Command Language version 6.5.0 (UCAR/NCAR/CISL/TDD 2018).

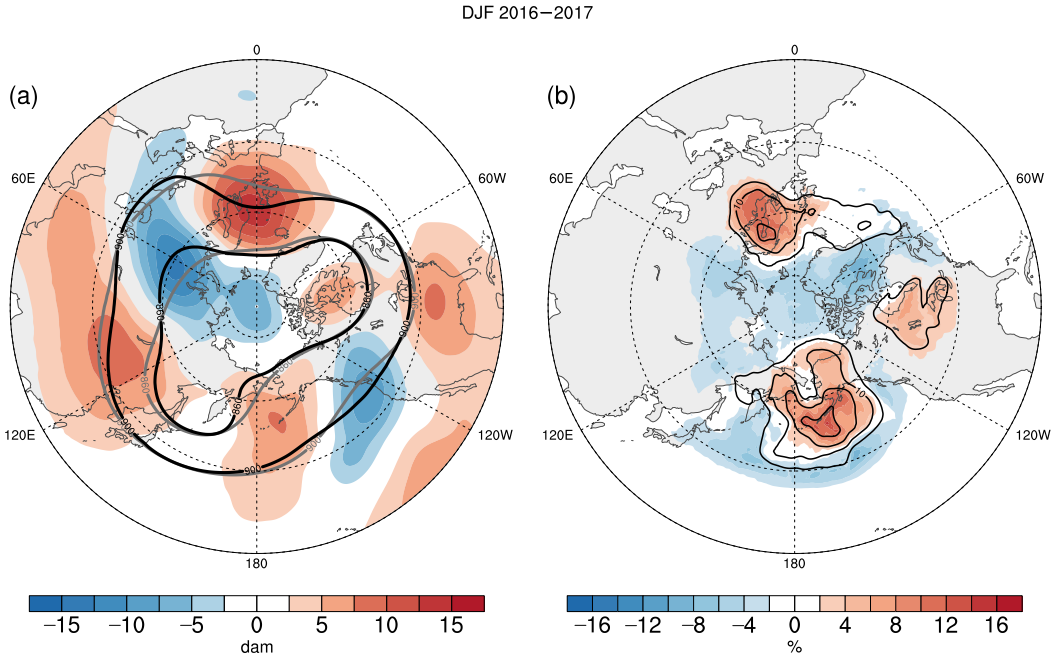


FIG. 5. Analyses for December 2016–February 2017 showing (a) time-mean 300-hPa geopotential height anomalies (shaded in dam) and (b) relative frequency (black contours every 5%) and relative frequency anomalies for blocking (shaded in %). Anomalies in (a),(b) are computed relative to the mean for prior winters during 1979–2015 exhibiting a multivariate ENSO index value of < –0.4. The 860-dam and 900-dam geopotential height contours for winter 2016–17 (black) and for the prior winters (gray) are overlaid in (a).

interaction of waves propagating along the two jets toward the U.S. West Coast. The trough along the polar jet was displaced immediately poleward and downstream of a broad trough along the subtropical jet (Fig. 6a), promoting southwesterly flow into the U.S. West Coast. Cyclone activity was focused within a southwest–northeast-oriented area over the eastern North Pacific in the vicinity of the two troughs (Fig. 6c). This area was flanked by a corridor of anomalous IVT extending into the California coast (see Fig. 3d), reflecting ARs linked to the cyclones. Warm conveyor belt activity (Fig. 6c), negative OLR anomalies, and upper-level divergent outflow (Fig. 6b) occurred over the eastern North Pacific and western North America, suggesting deep lifting of moist air in cyclone warm sectors.

### *b. Synoptic–dynamic diagnosis*

Figures 7–11 depict the evolution of the flow for the early February 2017 event. Between 31 January and 6 February, two successive episodes of baroclinic development, manifested by strong cyclogenesis, cyclonic wave breaking, and downstream ridge amplification, occurred over the western North Pacific (Figs. 7a–e, 8a–e). The ridge amplification, marked by strong poleward wave activity flux, supported growth and persistence of the blocking ridge. The latter of the two episodes was instigated during 2–3 February as a wave packet (red arrows; Figs. 7a–c, 9a) propagated southeastward across Asia along the polar jet and interacted with the subtropical jet over the western North Pacific. This wave packet originated in a region of anticyclonic wave breaking over north-central Asia downstream of an amplifying ridge over northern Europe (Fig. 7a). Between 2 and 7 February (Figs. 7b–f), anticyclonic wave breaking occurred in conjunction with strong southeastward wave activity flux on the eastern flank of the block, resulting in the formation of slow-moving positively tilted PV streamers (i.e., troughs) across the northwestern coast of North America and the Gulf of Alaska. This wave breaking resulted in the establishment and maintenance of strong baroclinicity over the northwestern United States and western Canada (Figs. 8b–f).

Between 2 and 7 February, three successive cyclones, labeled L1, L2, and L3, respectively, moved across the eastern North Pacific equatorward of the block and impacted the U.S. West Coast (Figs. 8b–f). L1 was associated with a preexisting cut-off disturbance

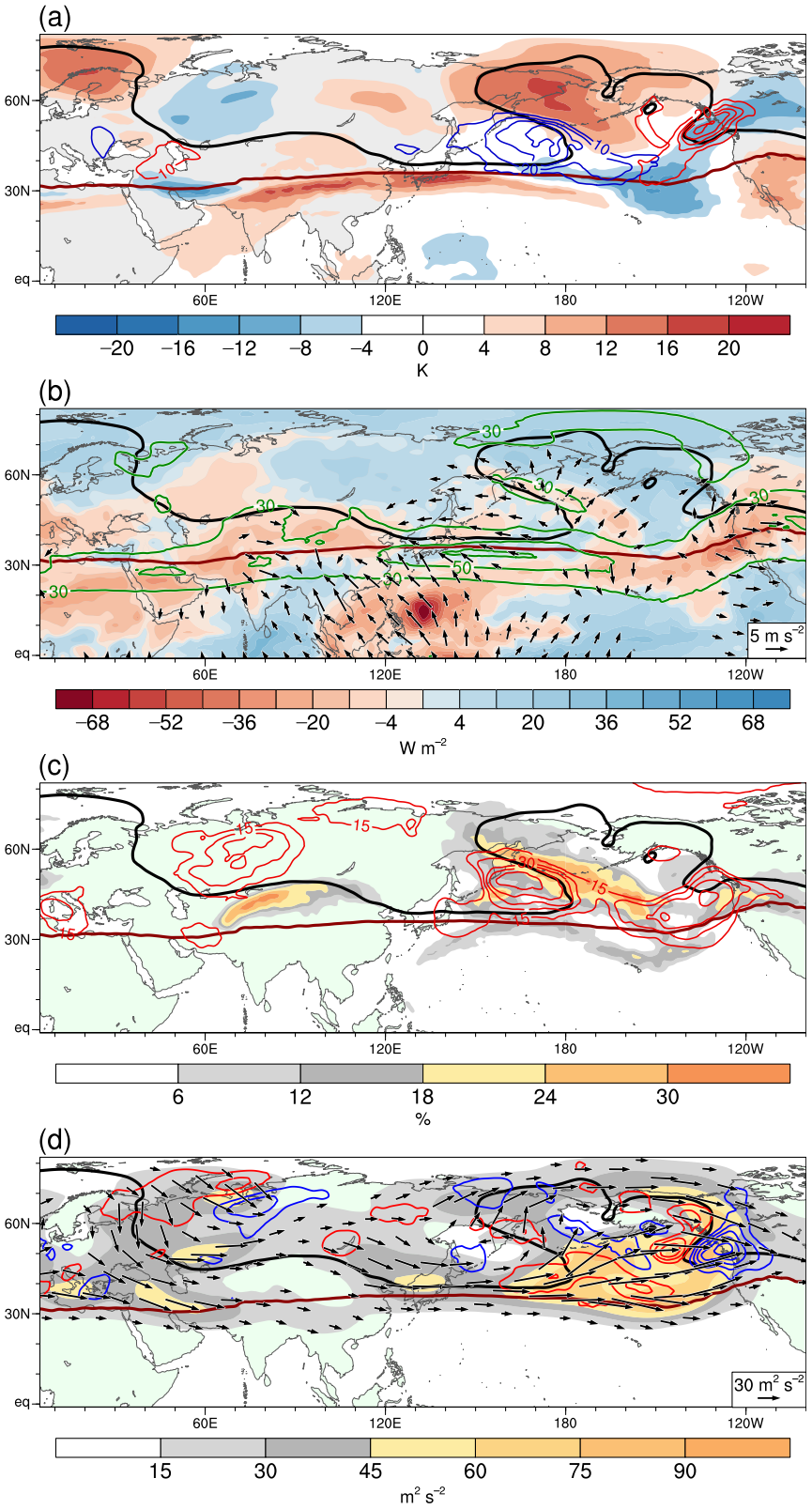


FIG. 6. Analyses for 1–10 Feb 2017. (a) Time-mean dynamic tropopause $\theta$ anomalies (shaded in K) and the relative frequency of cyclonic (blue contours every 10%) and anticyclonic

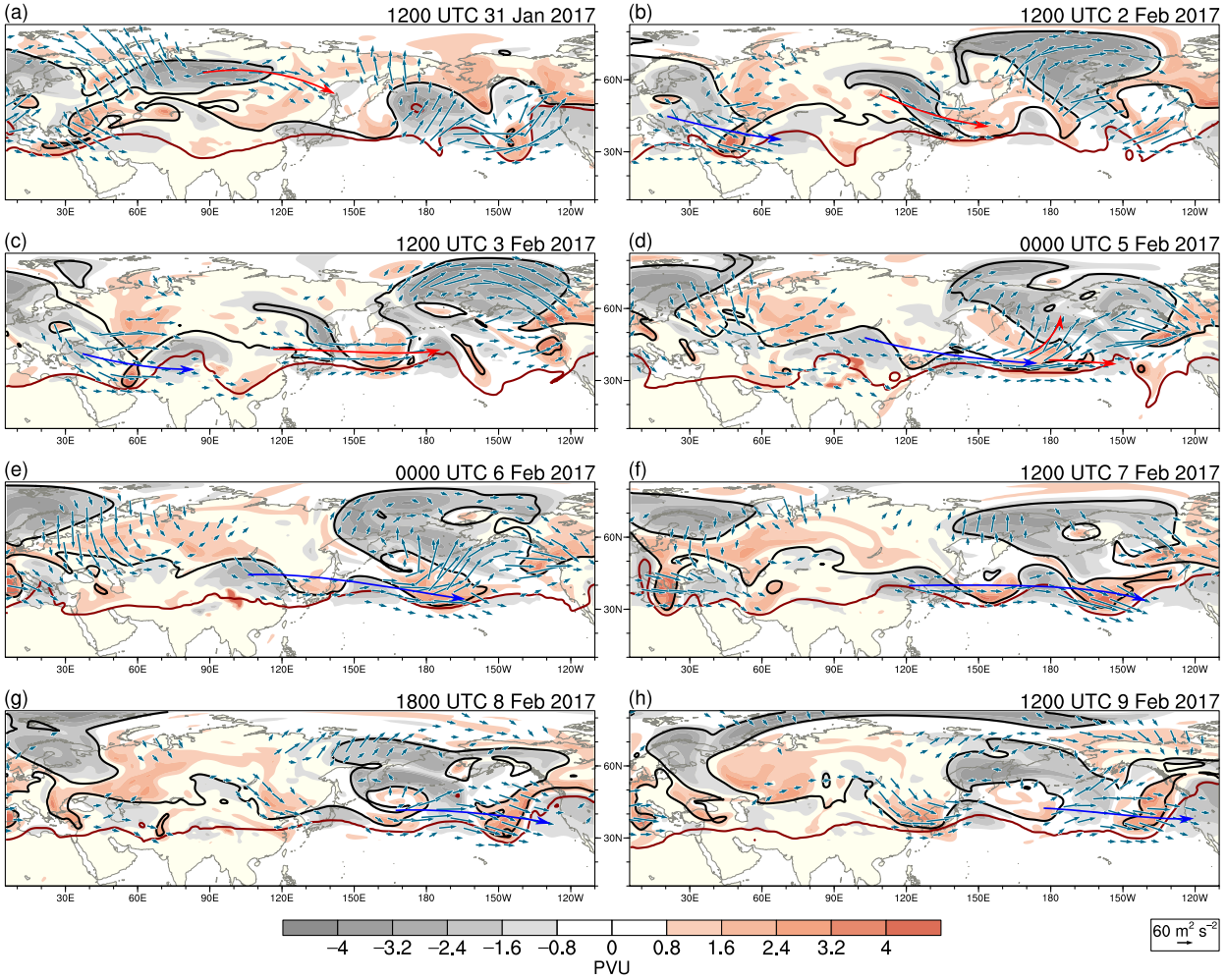


FIG. 7. 310–330-K layer-averaged PV anomalies (shaded in PVU), the 2-PVU contour on the 310-K (black) and 330-K (red) surfaces, and 350–250-hPa layer-averaged wave activity flux (vectors for magnitudes $\geq 30\ m^2\ s^{-2}$, reference vector in lower right) for (a) 1200 UTC 31 Jan, (b) 1200 UTC 2 Feb, (c) 1200 UTC 3 Feb, (d) 0000 UTC 5 Feb, (e) 0000 UTC 6 Feb, (f) 1200 UTC 7 Feb, (g) 1800 UTC 8 Feb, and (h) 1200 UTC 9 Feb 2017. Two Rossby wave packets discussed in the text are subjectively marked by red and blue arrows, respectively.

over the eastern North Pacific (Fig. 8a). L2 and L3 developed on 2 and 6 February (Figs. 8b,e), respectively, near the tips of negatively tilted PV streamers that stretched into the eastern North Pacific as a result of successive cyclonic wave breaking episodes on the upstream flank of the block. The three cyclones each tracked eastward across the eastern North Pacific in association with apparent wave

←

(red contours every 10%) wave breaking PV streamers on the 310-K surface. (b) Time-mean OLR anomalies (shaded in $W\ m^{-2}$), 250-hPa irrotational wind (vectors for magnitudes $\geq 2\ m\ s^{-1}$, reference vector in lower right), and dynamic tropopause wind speed (green contours every $20\ m\ s^{-1}$ starting at $30\ m\ s^{-1}$). (c) Relative frequency of extratropical cyclones (red contours every 15%) and warm conveyor belt outflows (shaded in %). (d) Time-mean 350–250-hPa layer-averaged wave activity flux (magnitude shaded in $m^2\ s^{-2}$; vectors for magnitudes $\geq 15\ m^2\ s^{-2}$, reference vector in lower right) and wave activity flux divergence (every $2.5 \times 10^{-5}\ m\ s^{-2}$, positive values in red and negative values in blue). In (a)–(d), the time-mean 2-PVU contours on the 310-K (thick black) and 330-K (thick dark red) surfaces depict the configuration of the polar and subtropical jets, respectively.

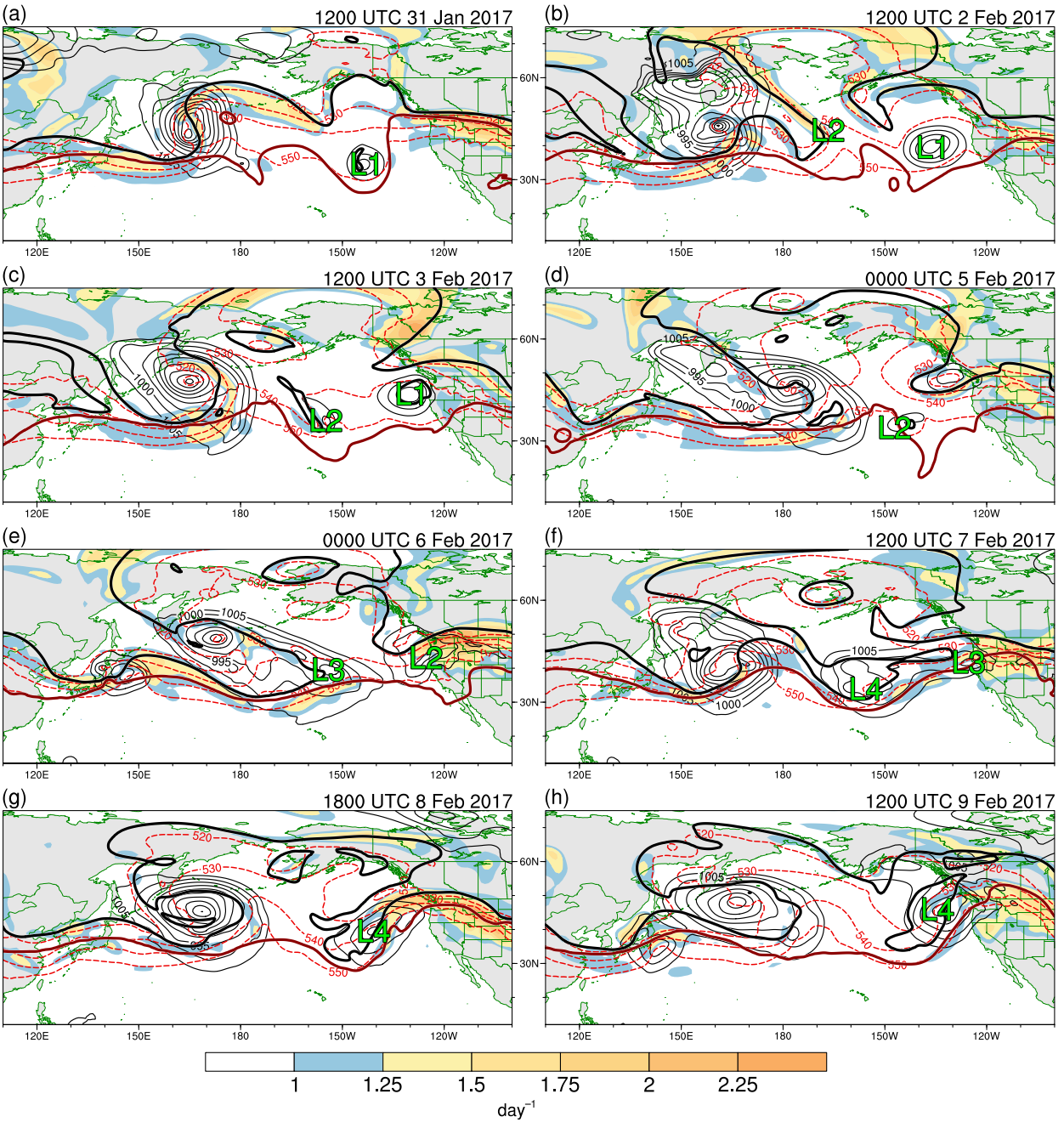


FIG. 8. 700-hPa Eady growth rate (shaded in day$^{-1}$), sea level pressure (thin black contours every 5 hPa at and below 1005 hPa), 1000–500-hPa thickness (dashed red contours every 10 dam between 520 and 550 dam), and the 2-PVU contour on the 310-K (thick black) and 330-K (thick dark red) surfaces for (a) 1200 UTC 31 Jan, (b) 1200 UTC 2 Feb, (c) 1200 UTC 3 Feb, (d) 0000 UTC 5 Feb, (e) 0000 UTC 6 Feb, (f) 1200 UTC 7 Feb, (g) 1800 UTC 8 Feb, and (h) 1200 UTC 9 Feb 2017. In (a)–(h), locations of the sea level pressure minima for cyclones L1, L2, L3, and L4 are indicated.

packets along the subtropical jet (green arrows in Fig. 9b). On the downstream flank of the block near the U.S. West Coast, the cyclones each interacted with a positively tilted PV streamer and an associated baroclinic zone linked to anticyclonic wave breaking (Figs. 8b–f). The interactions resulted in forcing of upward $\omega_{QG}$ and supported intensification and eastward movement of the cyclones (Figs. 10a–d). The landfall of L1, L2, and L3 enabled accompanying ARs, manifested by regions of strong IVT (>300 kg m$^{-1}$ s$^{-1}$)

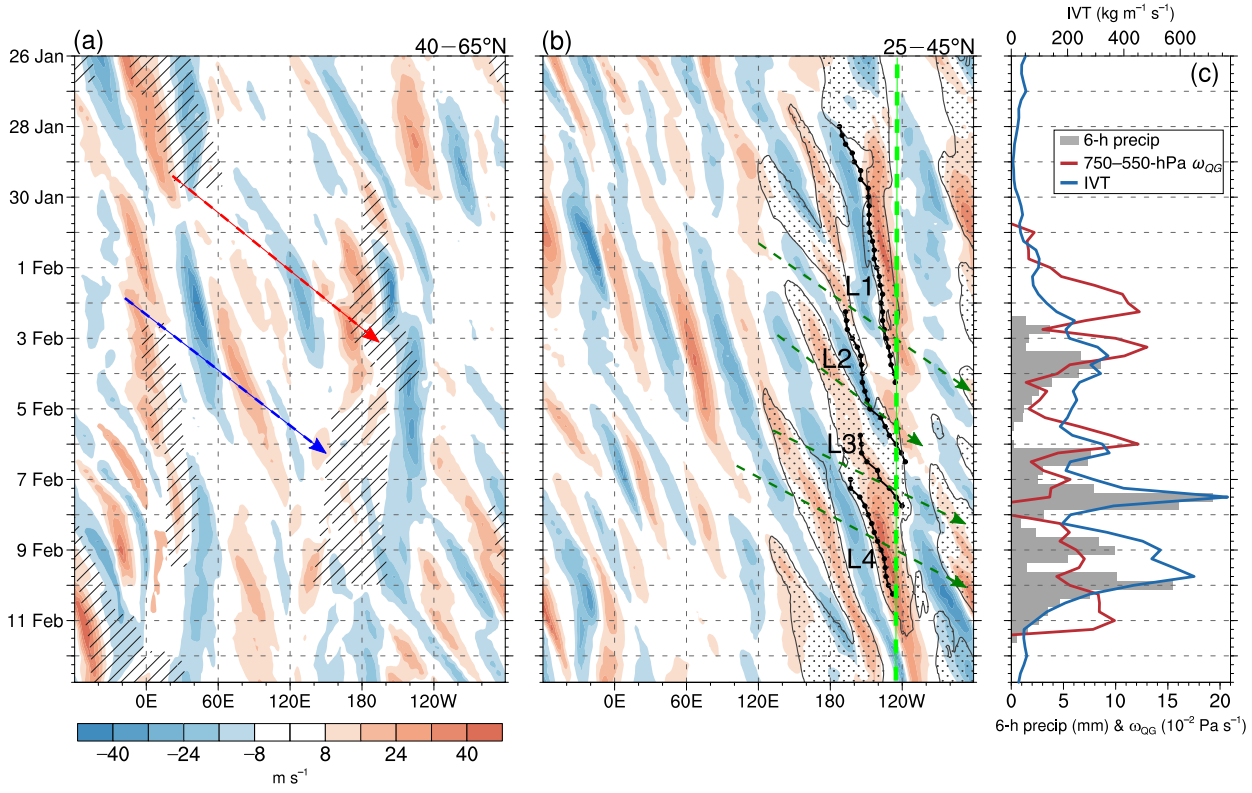


FIG. 9. Hovmöller diagrams for 26 Jan–12 Feb 2017 depicting (a) averaged 310-K meridional wind anomalies (shaded in m s$^{-1}$) and blocking occurrences (hatching) in the 40°–65°N band, and (b) averaged 330-K meridional wind anomalies (shaded in m s$^{-1}$) and maximum IVT magnitude (stippling for values of >400 kg m$^{-1}$ s$^{-1}$) in the 25°–45°N band. (c) Time series for 26 Jan–12 Feb 2017 of 750–550-hPa layer-averaged negative (i.e., upward) $\omega_{QG}$ (red curve), IVT magnitude (blue curve), and 6-h Stage-IV precipitation (gray bars) averaged within the Northern California domain depicted in Fig. 1c. In (b), the black lines and dots mark the tracks of cyclones L1, L2, L3, and L4, and the vertical dashed green line denotes the westernmost longitude of the Northern California domain depicted in Fig. 1c. Approximate group velocities of Rossby wave packets discussed in the text are subjectively indicated by red and blue arrows in (a) and by dark green arrows in (b).

and high IWV (20–30 mm), to impact Northern California (Figs. 11a–d).[4]

During 2–6 February, a wave packet along the polar jet (blue arrows; Figs. 7b–e, 9a) emerged from the eastern flank of a high-amplitude ridge over Europe and propagated across central and eastern Asia and into the western North Pacific. During 2–3 February (Figs. 7b,c), the wave packet extended southeastward in connection with anticyclonic wave breaking between ~30° and ~80°E and appeared to phase with and amplify a preexisting wave pattern along the subtropical jet. By 7 February (Fig. 7f), the wave packet, marked by a corridor of wave activity flux, had extended along both the polar and subtropical jets into the eastern North Pacific equatorward of the block. The signature of the wave packet along the subtropical jet is denoted by the bottommost arrow in Fig. 9b.

During 7–9 February, the wave packet underwent amplification via a process of downstream baroclinic development (e.g., Simmons and Hoskins 1979; Orlanski and Sheldon 1993). In this process, strong cyclogenesis, cyclonic wave breaking, and ridge amplification occurred over the western North Pacific on the upstream flank of the block (Figs. 8f–h). Wave activity was concurrently fluxed downstream from the ridge, corresponding to trough amplification immediately poleward of Hawaii. This amplification occurred in the western portion of a highly elongated negatively tilted PV streamer stretching equatorward of the block (Figs. 7f–h). The trough was associated with forcing of upward $\omega_{QG}$ and the concomitant development of a strong cyclone, L4, immediately upstream of L3 (Figs. 10d–f).

During 7–8 February (Figs. 7f–g), the upper-level trough associated with L4 merged with a positively tilted PV streamer over the Gulf of Alaska as ridge amplification occurred downstream due to warm-air advection and latent heating in the warm sector of L4 (not shown). This merger corresponded to increased

[4] The IWV from the ERA-Interim corresponds to the entire atmospheric column.

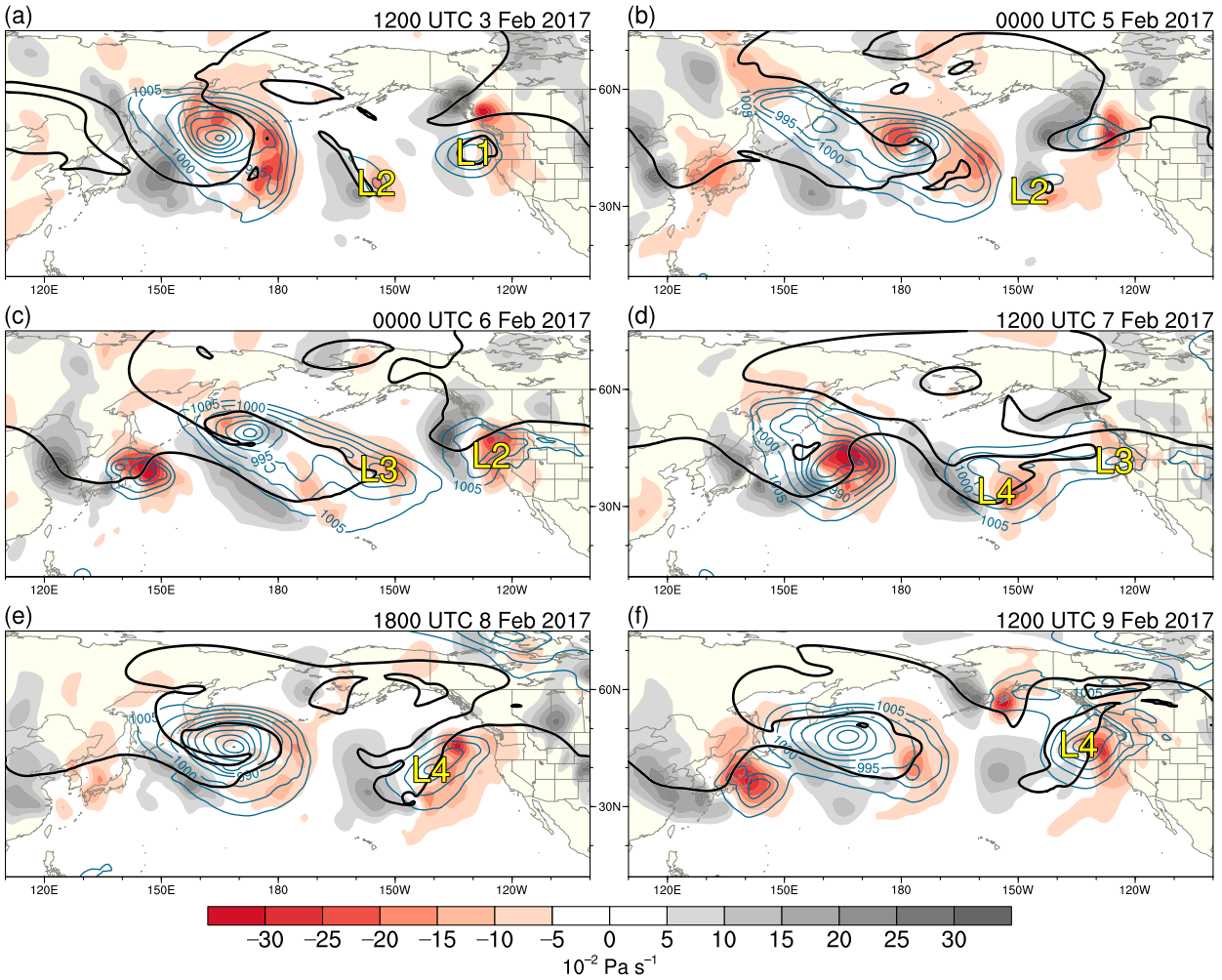


FIG. 10. 750–550-hPa layer-averaged $\omega_{QG}$ (shaded in $10^{-2}$ Pa s$^{-1}$), sea level pressure (blue contours every 5 hPa at and below 1005 hPa), and the 2-PVU contour on the 310-K surface (black) for (a) 1200 UTC 3 Feb, (b) 0000 UTC 5 Feb, (c) 0000 UTC 6 Feb, (d) 1200 UTC 7 Feb, (e) 1800 UTC 8 Feb, and (f) 1200 UTC 9 Feb 2017. In (a)–(f), locations of the sea level pressure minima for cyclones L1, L2, L3, and L4 are indicated.

baroclinicity (Figs. 8f,g) and strengthened upward $\omega_{QG}$ (Figs. 10d,e) over the central and eastern portions of L4, causing the cyclone to intensify and move northeastward toward the British Columbia coast. The development of L4 between 7 and 8 February coincided with the formation of a strong southwesterly AR (IVT of >300 kg m$^{-1}$ s$^{-1}$ and IWV of >30 mm; Figs. 11d,e) in its warm sector. This AR impacted Northern California during 8–9 February immediately after the AR associated with L3 (Figs. 11d–f).

Time series for Northern California (Fig. 9c) demonstrate nearly continuous moderate and strong IVT and upward $\omega_{QG}$ during 2–10 February 2017 as L1, L2, L3, and L4 impacted the U.S. West Coast in rapid succession (i.e., at ~24–48-h intervals; Fig. 9b). The latter two cyclones were associated with particularly strong IVT. The persistent lifting and water vapor supply sustained moderate and heavy precipitation in Northern California (Fig. 9c), culminating in extreme precipitation accumulations. The 9-day precipitation totals ranked above the 99th percentile of the 1979–2017 climatology over most of Northern California and above the 99.5th percentile in mountainous regions, including the Sierra Nevada (Fig. 12a). Extraordinary persistence of the water vapor transport supporting the precipitation is demonstrated by a corridor of extreme (>99.5th percentile) 9-day time-integrated IVT extending into Northern California (Fig. 12b).

### c. *Mesoscale diagnosis*

Time series for 3–10 February 2017 demonstrate a close correspondence between the bulk upslope IWV

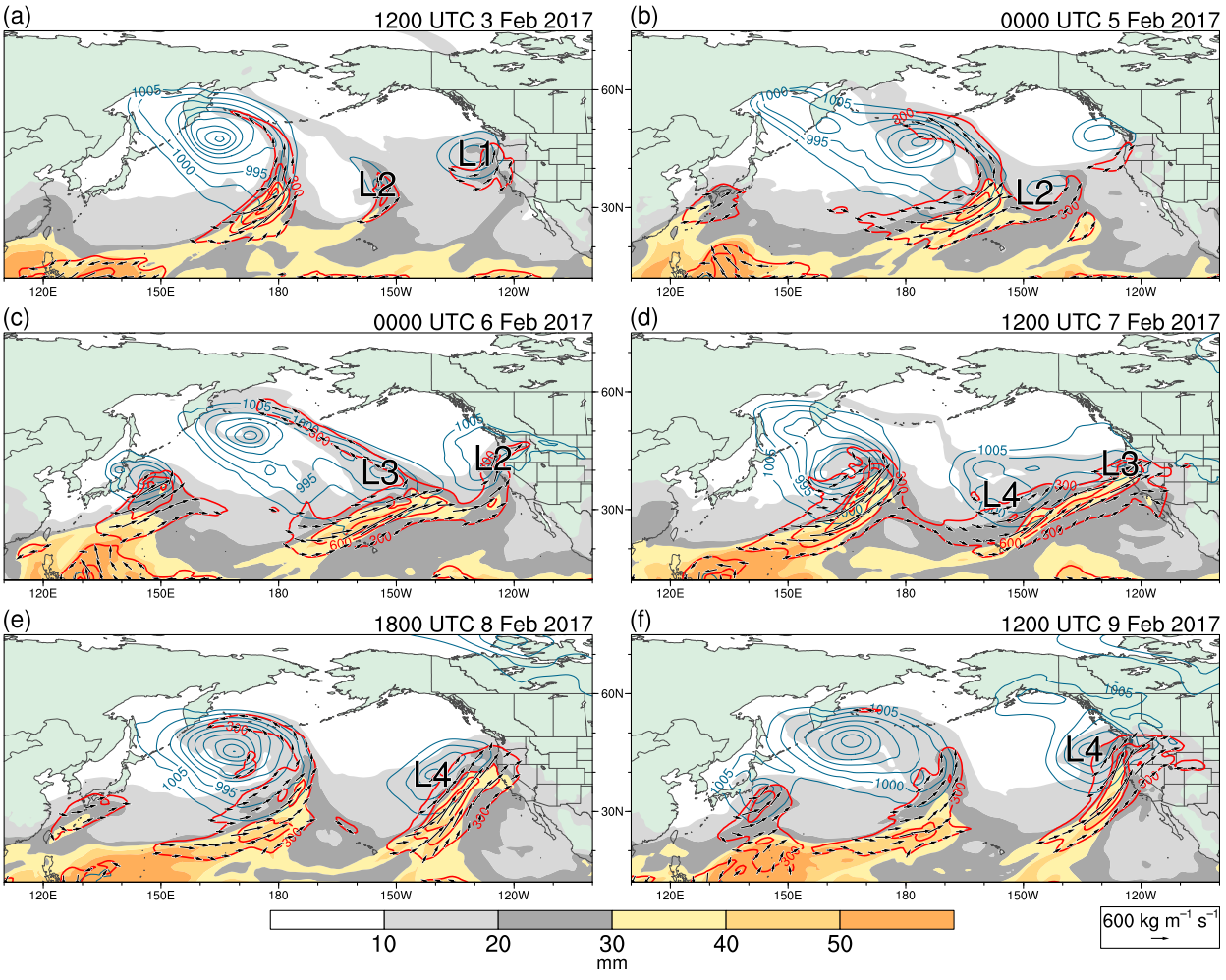


FIG. 11. IWV (shaded in mm), sea level pressure (blue contours every 5 hPa at and below 1005 hPa), and IVT (magnitude contoured in red every 300 kg m$^{-1}$ s$^{-1}$; vectors plotted for magnitudes ≥300 kg m$^{-1}$ s$^{-1}$, reference vector scale in the lower right) for (a) 1200 UTC 3 Feb, (b) 0000 UTC 5 Feb, (c) 0000 UTC 6 Feb, (d) 1200 UTC 7 Feb, (e) 1800 UTC 8 Feb, and (f) 1200 UTC 9 Feb 2017. In (a)–(f), locations of the sea level pressure minima for cyclones L1, L2, L3, and L4 are indicated.

flux and precipitation for the BBY–ANG and CCO–FOR station pairs (Fig. 13a). Particularly strong flux and heavy precipitation occurred during 7–9 February in association with L3 and L4. The upslope flux at BBY and CCO is plotted for the 1.0–1.5 km MSL and 1.5–2.0 km MSL layers, respectively, where the BBY–ANG and CCO–FOR flux–precipitation correlations maximize (Fig. 13b). The maximum correlations for the two pairs of sites were 0.81 and 0.73, respectively (Fig. 13b), signifying strong orographic modulation of the precipitation.

Time-mean maps for 6–10 February from the HRRR analyses depict strong southwesterly IVT for the surface–700-hPa layer impinging upon the Northern California coast (Figs. 13c,d), reflecting the collective effects of the ARs linked to L2, L3, and L4. Precipitation totals of >25 mm were widespread across Northern California (Fig. 13d), consistent with synoptic-scale ascent forced in connection with the cyclones (Figs. 10c–f). Large totals (e.g., >100 mm; Fig. 13d) were focused where the IVT strongly impinged on areas of elevated terrain (Fig. 13c), including the Coast Ranges, the Sierra Nevada, and the mountains at the northern end of the Central Valley. The IVT affecting the latter two regions occurred within a corridor that extended through the San Francisco Bay Area terrain gap and poleward in the Central Valley (Fig. 13c). This corridor signifies inland water vapor transport as the ARs made landfall (e.g., White et al. 2015).

## 5. Climatological perspective

The foregoing case study highlights multiscale aspects of a long-duration EPE in Northern California involving

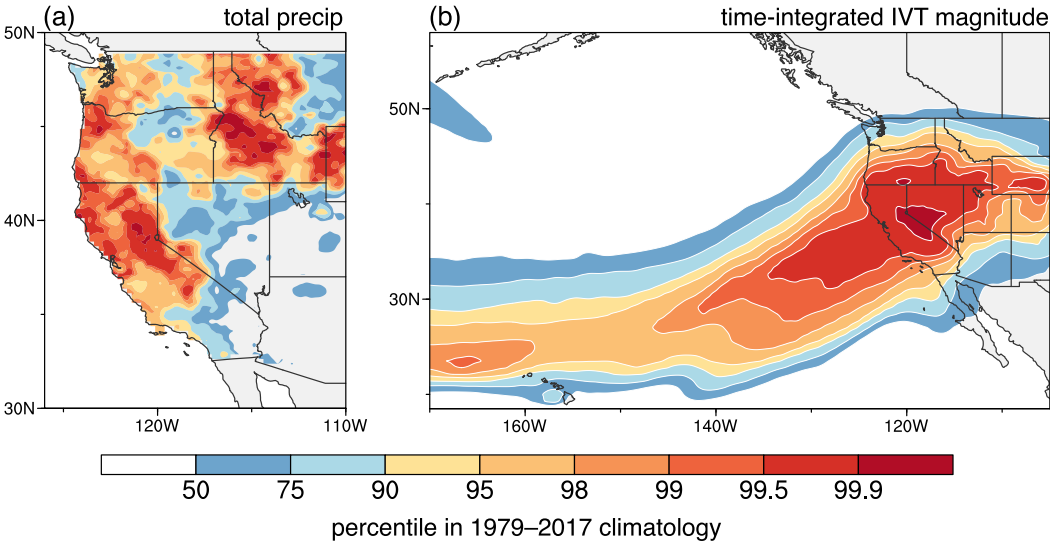


FIG. 12. Percentile ranking in the 1979–2017 climatology of the (a) total UPD precipitation and (b) time-integrated IVT magnitude for 2–10 Feb 2017. Values are calculated at each grid point relative to a distribution of all 9-day periods during 1979–2017.

Bering Sea–Alaska blocking. The generalizability of the case study findings is, however, limited. Here, a climatological analysis is performed to explore the hypothesis that Bering Sea–Alaska blocking is conducive to the occurrence of EPEs in Northern California.

### *a. Climatology methods*

A climatology of blocking events analogous in spatial scale and location to the early February 2017 blocking event was constructed for an extended winter period, November–March, for 1979–2017 using the blocking dataset from Sprenger et al. (2017; see Table 1). To select the events, a mask (hatching in Fig. 14) was defined that was composed of grid points at which blocking occurred during 3–9 February 2017. For each day in the extended winter, the fraction of the grid points in the mask overlapped by a block was determined. All days on which a block overlapped the mask were then sorted by this fraction, and the top quintile (fraction threshold of ~27%; 613 days) were designated as blocking days. All other days (5283 days) were designated as nonblocking days. Consecutive blocking days were considered to comprise the same event. In total, 135 distinct blocking events were identified. For reference, the composite 300-hPa geopotential height field for these events is shown in Fig. 14.

The relationship between blocking and extreme precipitation was quantified using the odds ratio [Wilks 2011, section 8b(2)]:

$$\text{odds ratio} = \frac{P(E|B)[1 - P(E|B)]^{-1}}{P(E|N)[1 - P(E|N)]^{-1}}, \qquad (2)$$

where $P(E|B)$ and $P(E|N)$ denote the conditional probabilities of an EPE given that blocking does and does not occur, respectively. This metric quantifies the ratio of the odds of an EPE for blocking conditions to the odds for nonblocking conditions and thereby measures the strength of the statistical association between blocking and EPEs. A value greater (less) than unity indicates a positive (negative) statistical association, such that the odds of an EPE are enhanced (reduced) in blocking conditions relative to nonblocking conditions. A value of unity indicates that blocking and EPEs are statistically unrelated.

Using the UPD analyses, EPEs were identified in 1-, 3-, 5-, and 7-day accumulated precipitation time series at each grid point and precipitation volume time series for the Northern California domain. The multiday amounts were calculated as running accumulations and were assigned to the center day of the respective time periods. EPEs were defined as a precipitation amount exceeding the 99th percentile of the 1979–2017 climatology. As in Lenggenhager and Martius (2019), the multiday EPE samples were filtered to obtain subsets of approximately independent events for the odds ratio calculations. Sequential multiday events that overlapped by $\geq M$ days were flagged, and only the event with the most precipitation was retained. For the 3-, 5-, and 7-day events, $M$ was set to 1, 2, and 3, respectively. The conditional probabilities in Eq. (2) were calculated as the fraction of blocking or nonblocking days on which an EPE occurred. The null hypothesis that the odds ratio equals unity was tested using a 1000-iteration bootstrap resampling technique (Wilks 2011, his section 5.3.5).

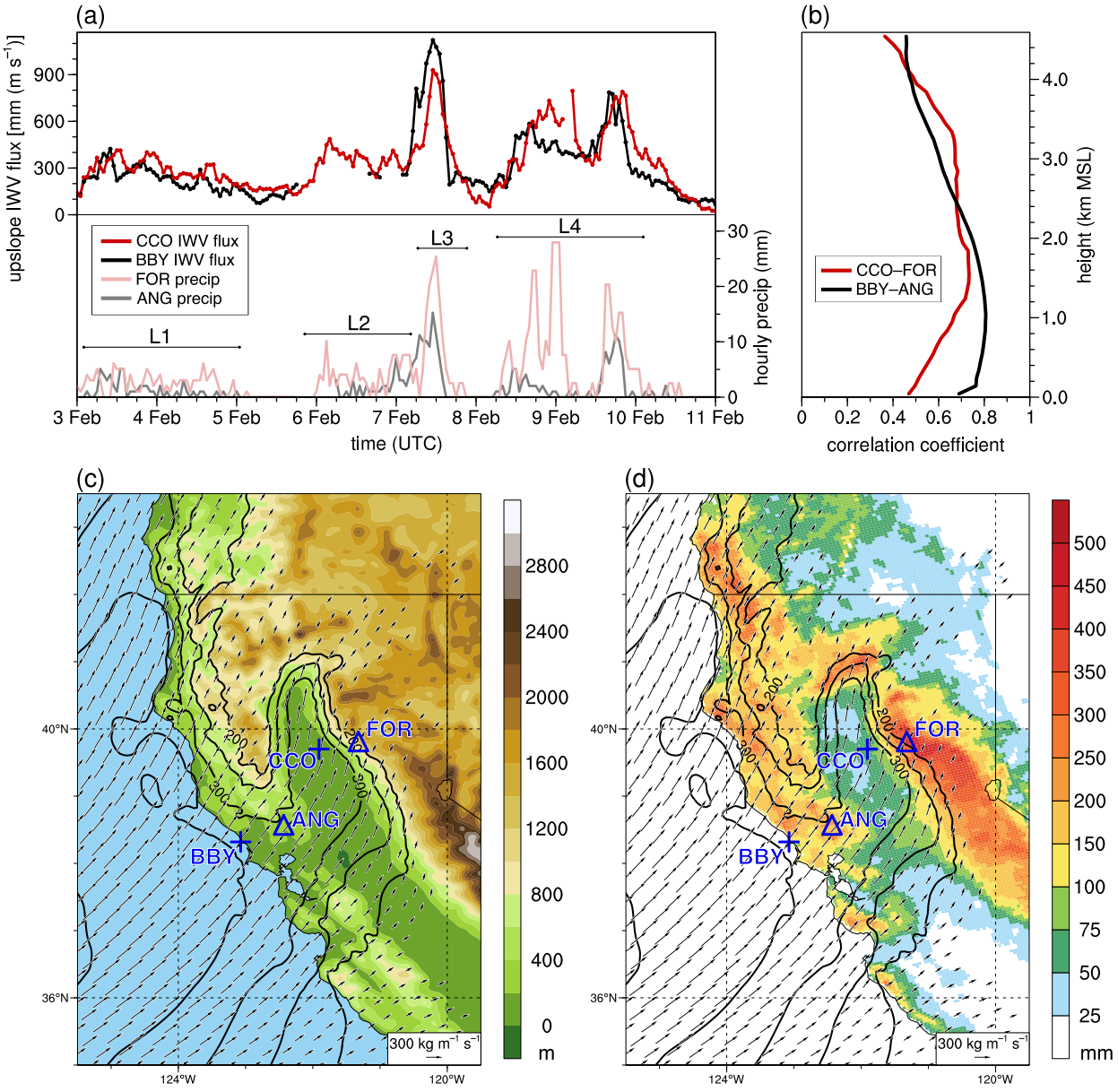


FIG. 13. (a) Hourly time series of the bulk upslope (wind direction: 230°) IWV flux averaged for the 1.5–2.0 km MSL layer at CCO (red curve) and the 1.0–1.5 km MSL layer at BBY (black curve), and precipitation at FOR (pink curve) and ANG (gray curve). Approximate time ranges for L1, L2, L3, and L4 are indicated. (b) Pearson correlation coefficient with respect to height of the bulk upslope IWV flux and precipitation time series for the CCO–FOR and BBY–ANG station pairs. The correlations are computed for the upslope flux averaged in overlapping 500-m vertical layers, as in Neiman et al. (2002). The ordinate in (b) corresponds to the lower bounds of the 500-m layers. (c) Terrain elevation (shaded in m) overlaid by the time-mean surface–700-hPa IVT (black contours every 100 kg m$^{-1}$ s$^{-1}$ starting at 200 kg m$^{-1}$ s$^{-1}$; vectors for magnitudes ≥150 kg m$^{-1}$ s$^{-1}$, reference vector in lower right) for 6–10 Feb 2017 from the HRRR analyses. (d) As in (c), but showing the IVT overlaid on the Stage-IV accumulated precipitation (shaded in mm) for 6–10 Feb 2017. The locations of BBY, ANG, CCO, and FOR are indicated in (c),(d).

Composite analyses were constructed for blocking events that co-occurred with a 5-day EPE based on Northern California precipitation volume (19 events). For the composites, a reference time, $t_0$, was defined as 0000 UTC on the center day of the EPE. Statistical significance of composite anomalies was determined through a 1000-sample bootstrap test of the null hypothesis that the difference in the mean between the blocking sample and the corresponding climatology is zero. Statistical significance for relative frequency anomalies of PV streamers and cyclones was determined through a 1000-sample Monte Carlo test, as described in Scherrer et al. (2006).

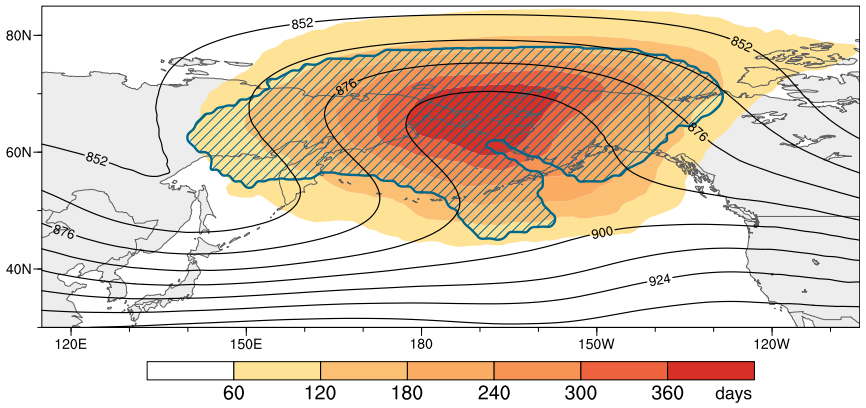


FIG. 14. The mask used to select blocking events (blue hatching; see text), the number of days on which blocking occurred as part of the selected blocking events (shading), and the composite 300-hPa geopotential height field (contours every 12 dam) for the blocking events.

### b. *Climatology results*

Odds ratios of EPEs in Northern California are statistically significant and greater than unity for all durations (Table 2). Furthermore, appreciable fractions (~21%–43%) of the EPEs co-occur with blocking (Table 2). The odds ratios and co-occurrence fractions are considerably larger for the 5- and 7-day EPEs than for the 1- and 3-day EPEs, indicating particularly strong relevance of blocking to long-duration events. The fraction of the distinct blocking events that co-occurred with an EPE was generally constant at ~13%–14% (18–19 of 135 events) for the different durations. In aggregate, ~19% (25 of 135 events) of the blocking events co-occurred with any EPE.

Maps of odds ratios for 1- and 5-day EPEs and extreme (>99th percentile) time-integrated IVT occurrences (Fig. 15) complement the results in Table 2. For 1-day EPEs, statistically significant odds ratios exceeding unity (values of 2–4) cover much of California, particularly the northern part (Fig. 15a). In general, the highest values are focused in mountainous regions, reflecting orographic enhancement. A similar pattern exists for the 5-day EPEs, though the values are generally higher and are less often statistically significant (Fig. 15b). Statistically significant odds ratios of extreme 1- and 5-day time-integrated IVT in excess of unity occur within elongated areas stretching across the subtropical and midlatitude eastern North Pacific into California (Figs. 15c,d). These signatures highlight a tendency for the blocking events to result in strong and persistent water vapor transport into California in connection with ARs. Odds ratios of EPEs and extreme IVT also exceed unity across portions of the Intermountain West (Figs. 15a–d), suggestive of inland water vapor transport linked to landfalling ARs (e.g., Rutz et al. 2014; Alexander et al. 2015).

The composite flow pattern for the blocking events associated with EPEs (Fig. 16) closely resembles that for the early February 2017 event (cf. to Fig. 6). Positive relative frequency anomalies of cyclonic wave breaking PV streamers and extratropical cyclones stretch eastward across the North Pacific equatorward of the block along a band negative dynamic tropopause $\theta$ anomalies (Figs. 16a,b). This configuration suggests a tendency for eastward elongation of negatively tilted streamers and corresponding eastward movement of accompanying cyclones equatorward of the block, as occurred during the February 2017 event. Moreover, the anomalous cyclone activity extends toward the U.S. West Coast and is focused downstream of an elongated region of negative dynamic tropopause $\theta$ anomalies linked to anomalous anticyclonic wave breaking activity (Figs. 16a,b). The cyclone activity is associated with an expansive area of negative sea level pressure anomalies over the eastern North Pacific and a corridor of anomalous IVT extending into California (Fig. 16c). Analogous composite analyses for null blocking events (not shown), defined as events during which the 5-day precipitation volume in

TABLE 2. The odds ratio of EPEs for the blocking days relative to the nonblocking days, and the fraction of the EPEs that co-occurred with blocking (in %, rounded to the nearest whole number). EPEs are identified based on 1-, 3-, 5-, and 7-day accumulated precipitation volumes in the Northern California domain (Fig. 1c). All odds ratio values are statistically significant at the 95% confidence level.

| EPE duration (days) | Odds ratio | Co-occurrence fraction (%) |
|---|---|---|
| 1 | 2.59 | 21 |
| 3 | 3.18 | 25 |
| 5 | 6.76 | 43 |
| 7 | 6.42 | 42 |

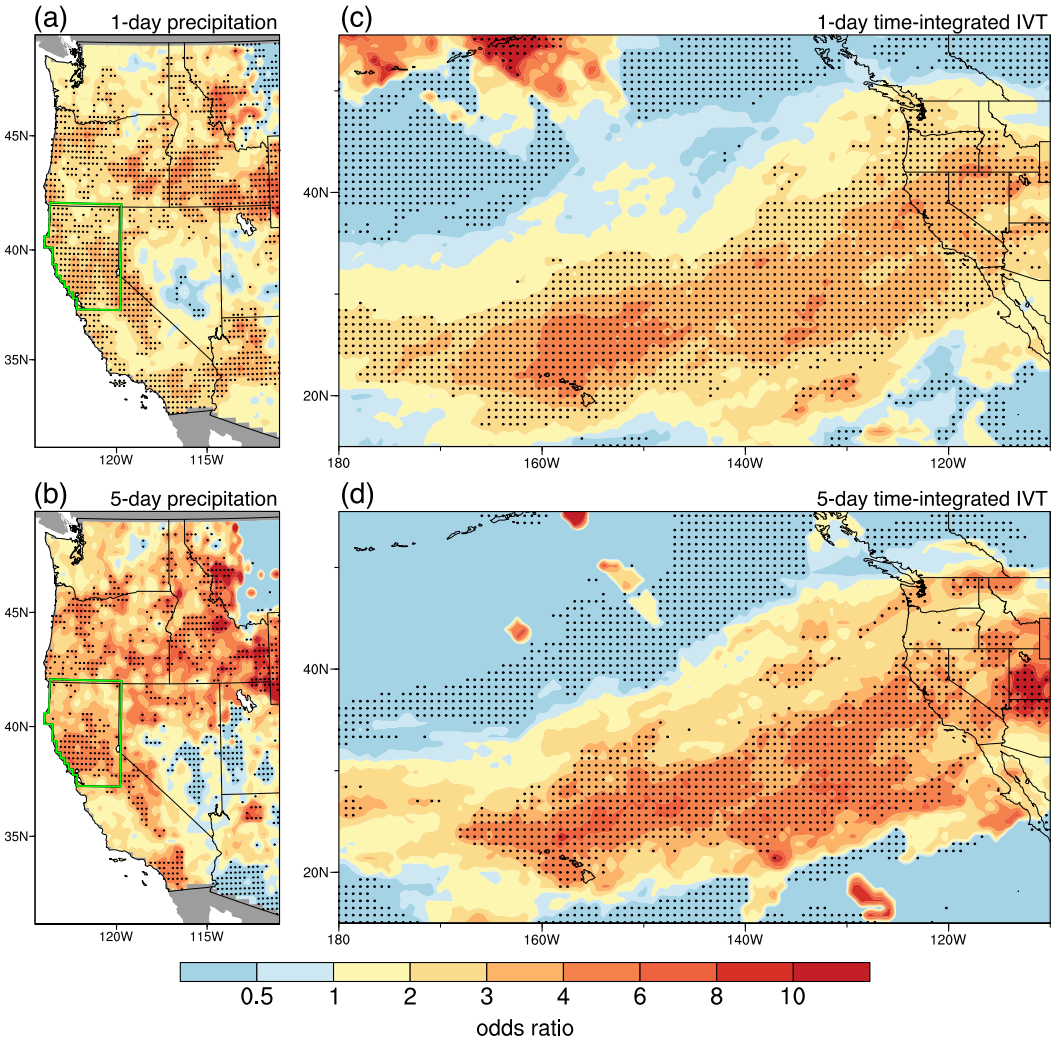


FIG. 15. Odds ratios of (a) 1-day and (b) 5-day EPEs, and extreme (>99th percentile) (c) 1-day and (d) 5-day time-integrated IVT magnitude for the blocking days relative to the nonblocking days. In (a),(b), the Northern California domain is outlined in green. Grid points at which the value is statistically significant at the 95% confidence level are marked by block dots.

Northern California did not exceed the climatological 75th percentile, exhibit markedly different patterns of wave breaking and cyclone activity. These events tend to lack the PV streamer activity on the equatorward and downstream flanks of the block. Accordingly, anomalous cyclone activity and IVT is absent along the U.S. West Coast.

A composite Hovmöller diagram of 310-K meridional wind anomalies for 45°–65°N for the EPE-related events illustrates the persistence (~12 days) of the blocking pattern (Fig. 17a). Anomalies on the 330-K surface for 25°–45°N depict signatures of multiple successive synoptic-scale waves propagating into the U.S. West Coast on the equatorward and downstream flanks of the block between $t_0 - 6$ days and $t_0 + 4$ days (Fig. 17a). These successive waves are associated with sustained anomalous cyclone activity and anomalous IVT along the coast (Fig. 17b).

## 6. Summary and discussion

During winter 2016–17, a series of long-duration EPEs caused hazardous flooding, provided beneficial water resources, and contributed substantially (~85%) to highly anomalous winter precipitation totals in Northern California. The three largest of these EPEs, occurring in mid-December, early January, and early February, respectively, involved high-amplitude large-scale flow patterns featuring blocking over the Bering Sea–Alaska region. A detailed multiscale investigation,

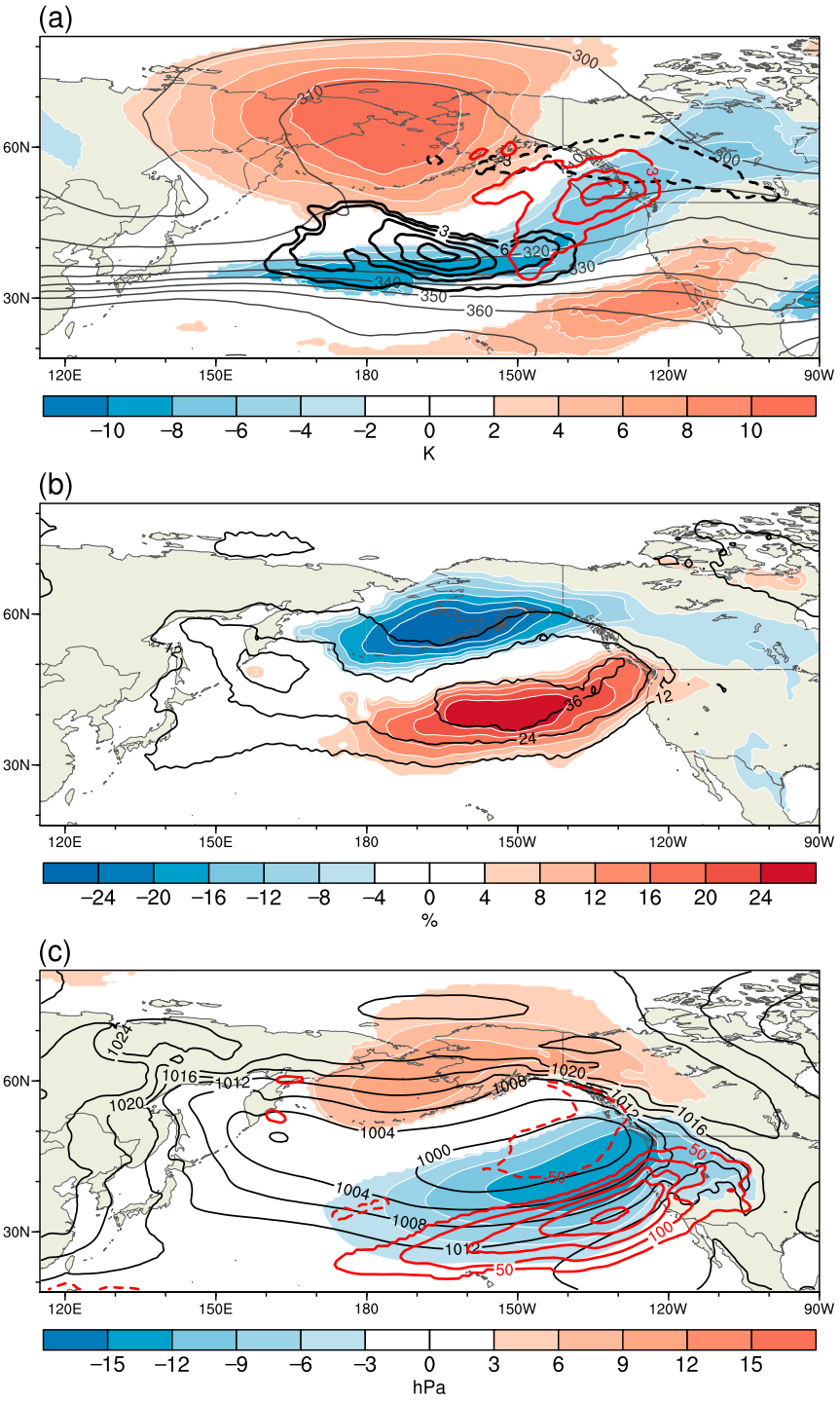


FIG. 16. Composite analyses for the 19 blocking events associated with a 5-day EPE in Northern California. (a) Dynamic tropopause $\theta$ (gray contours every 10 K), dynamic tropopause $\theta$ anomalies (shaded in K), and relative frequency anomalies (contours every 3%, dashed for negative values) of cyclonic (black) and anticyclonic (red) wave breaking PV streamers on the 310-K surface. (b) Relative frequency (black contours every 12%) and relative frequency anomalies (shaded in %) of extratropical cyclones. (c) Sea level pressure (black contours every 4 hPa), sea level pressure anomalies (shaded in hPa), and IVT anomalies (red contours ever 50 kg m$^{-1}$ s$^{-1}$, dashed for negative values). In (a)–(c), analyses are constructed for $t_0 - 60$ to $t_0 + 60$ h, and only anomaly values that are statistically significant at the 95% confidence level are plotted.

primarily focused on the early February 2017 event, was conducted to identify and diagnose processes associated with the blocking-related EPEs. A climatological analysis was then conducted for 1979–2017 to quantify and characterize the relationship between Bering Sea–Alaska blocking events and EPEs in Northern California.

The recurrence of the Bering Sea–Alaska blocking patterns throughout the winter was critical for the anomalous winter precipitation in Northern California. These patterns were possibly related to large-scale extratropical Rossby wave responses to tropical convection centered over the Maritime Continent linked to weak La Niña conditions and MJO activity, as suggested by Dong et al. (2018). However, the frequency of blocking over the central and eastern North Pacific during winter 2016–17 was considerably higher than the mean for prior La Niña winters. Moreover, the MJO appeared influential for only the early February blocking event. Thus, tropical convective forcing appears insufficient to explain the proclivity of the planetary-scale flow for the recurrence of the blocking. Factors accounting for this proclivity are unclear and warrant further investigation.

For the early February 2017 event, an expansive blocking ridge developed and persisted in conjunction with repeated episodes of baroclinic development, manifested by strong cyclogenesis, cyclonic wave breaking, and ridge amplification, over the western and central North Pacific. The baroclinic development was instigated as Rossby wave packets along the polar jet propagated across eastern Asia and interacted with the subtropical jet over the western North Pacific. Strong PV gradients and enhanced baroclinicity were supported in this region in connection with upper-level divergent outflow from MJO-related convection centered over the Maritime Continent. Anticyclonic wave breaking occurred on the downstream flank of the block, resulting in the formation of persistent positively tilted upper-level PV streamers (i.e., troughs) over northwestern North America and the Gulf of Alaska.

Synoptic-scale wave propagation across the North Pacific was focused in two main corridors on the poleward and equatorward flanks of the block, respectively. Propagation in the latter corridor enabled four successive cyclones to traverse the eastern North Pacific and make landfall along the U.S. West Coast during 2–10 February 2017, culminating in extreme precipitation in Northern California. An active storm track established equatorward of a block has been found previously (Weaver 1962; Carrera et al. 2004) to be a key feature of blocking-related EPEs in California.

The latter three cyclones developed and tracked across the eastern North Pacific in connection with the formation and eastward elongation of negatively tilted PV streamers equatorward of the block. These streamers formed in association with cyclonic wave breaking on the upstream flank of the block. As the four cyclones approached the downstream flank of the block, each interacted with a positively tilted PV streamer and an associated baroclinic zone established over northwestern North America through anticyclonic wave breaking. During the interactions, the cyclones intensified and tracked into the U.S. West Coast, enabling accompanying ARs to impact Northern California. Sequential periods of moderate and heavy precipitation occurred in Northern California during 2–10 February as moist air in the ARs was lifted in conjunction with synoptic-scale dynamical forcing tied to the cyclones and local orographic forcing along elevated terrain.

Consistent with findings of prior case studies (e.g., Martius et al. 2013; Grams et al. 2014; Barton et al. 2016; Lenggenhager et al. 2019), synoptic-scale Rossby wave breaking, manifested by the formation of PV streamers, played a central dynamical role in the nexus between extreme precipitation and the Bering Sea–Alaska blocking. A distinctive aspect of the scenario documented herein is that contemporaneous cyclonic and anticyclonic wave breaking, linked to the growth and persistence of a large-scale blocking pattern, acted in concert to promote serial clustering of cyclones, resulting in a long-duration EPE. Links between cyclone clustering and long-duration EPEs have also been documented in case studies of events in Europe (e.g., Sodemann and Stohl 2013; Grams et al. 2014; Priestley et al. 2017b). We conjecture that this clustering process constitutes a principal dynamical pathway for the occurrence of long-duration EPEs.

The climatological analysis for 1979–2017 reveals a significant statistical relationship between Bering Sea–Alaska blocking and EPEs in Northern California. The blocking events in the climatology account for an appreciable fraction of EPEs in Northern California. Moreover, the odds of EPEs for blocking conditions are significantly higher compared to the odds of EPEs for nonblocking conditions. Lenggenhager and Martius (2019) recently presented qualitatively similar findings with respect to EPEs in Europe for North Atlantic blocking events. The 5- and 7-day EPEs in Northern California are more strongly related to blocking than the 1- and 3-day EPEs, indicating that blocking is particularly favorable for long-duration events. A significant statistical relationship also exists between Bering Sea–Alaska blocking and extreme time-integrated IVT over the

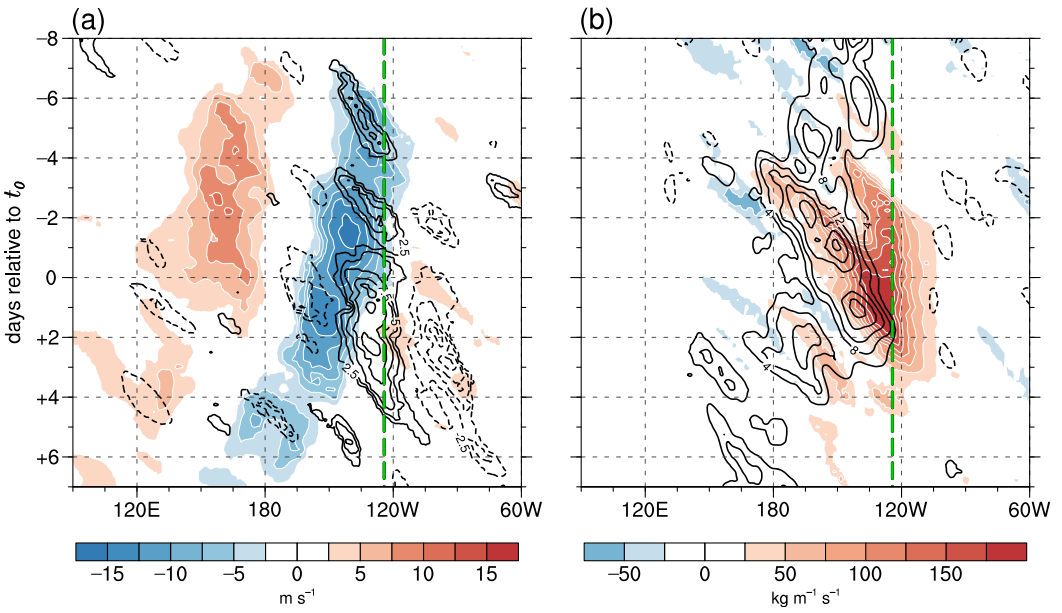


FIG. 17. Composite Hovmöller diagrams for the 19 blocking events associated with a 5-day EPE in Northern California. (a) Meridional wind anomalies on the 310-K surface averaged for 45°–65°N (shaded in m s$^{-1}$) and on the 330-K surface for 25°–45°N (black contours every 2.5 m s$^{-1}$, dashed for negative values). (b) IVT magnitude anomalies (shaded in kg m$^{-1}$ s$^{-1}$) and relative frequency anomalies of extratropical cyclones (black contours every 4%, dashed for negative values) averaged for 25°–45°N. Only anomaly values that are statistically significant at the 95% confidence level are plotted. The vertical dashed green line denotes the westernmost longitude of the Northern California domain depicted in Fig. 1c.

eastern North Pacific and California, suggesting a dynamical link between the blocking and strong, persistent AR conditions downstream. Composite analyses for blocking events in the climatology associated with 5-day EPEs in Northern California reveal a large-scale scenario that closely resembles that elucidated for the early February 2017 event.

We conclude by noting that the findings of the case study and the climatological analysis herein motivate additional research on EPEs in California, particularly those exhibiting long durations. Further composite analyses and detailed case studies could be performed to further investigate additional large-scale flow patterns and processes that may culminate in these events. Evaluation of medium-range and subseasonal forecasts for EPEs and associated large-scale flow patterns could also be performed to identify and diagnose relevant systematic forecast errors. These research avenues constitute critical steps for improving understanding and prediction of extreme precipitation in California.

*Acknowledgments.* Thanks go to Michael Sprenger and Heini Wernli (ETH-Zurich) for generously providing the blocking, cyclone, and warm conveyor belt climatologies, and to George Kiladis (NOAA/ESRL/PSD) and three anonymous reviewers for providing insightful comments on this manuscript. NOAA/ESRL's engineering and technical team built, deployed, and maintained the wind-profiling radars. The code for filtering OLR data was obtained from an online repository (https://k3.cicsnc.org/carl/monitor) maintained by Carl Schreck (NCICS). The NCAR Command Language version 6.5.0 was used for data processing, analysis, and visualization.

## REFERENCES

Alexander, M. A., J. D. Scott, D. Swales, M. Hughes, K. Mahoney, and C. A. Smith, 2015: Moisture pathways into the U.S. Intermountain West associated with heavy winter precipitation events. *J. Hydrometeor.*, **16**, 1184–1206, https://doi.org/10.1175/JHM-D-14-0139.1.

Altenhoff, A. M., O. Martius, M. Croci-Maspoli, C. Schwierz, and H. C. Davies, 2008: Linkage of atmospheric blocks and synoptic-scale Rossby waves: A climatological analysis. *Tellus*, **60A**, 1053–1063, https://doi.org/10.1111/j.1600-0870.2008.00354.x.

Appenzeller, C., and H. C. Davies, 1992: Structure of stratospheric intrusions into the troposphere. *Nature*, **358**, 570–572, https://doi.org/10.1038/358570a0.

Barlow, M., A. Hoell, and F. Colby, 2007: Examining the wintertime response to tropical convection over the Indian Ocean by modifying convective heating in a full atmospheric model. *Geophys. Res. Lett.*, **34**, L19702, https://doi.org/10.1029/2007GL030043.

Barton, Y., P. Giannakaki, H. von Waldow, C. Chevalier, S. Pfahl, and O. Martius, 2016: Clustering of regional-scale extreme

precipitation events in southern Switzerland. *Mon. Wea. Rev.*, **144**, 347–369, https://doi.org/10.1175/MWR-D-15-0205.1.

Benjamin, S. G., and Coauthors, 2016: A North American hourly assimilation and model forecast cycle: The Rapid Refresh. *Mon. Wea. Rev.*, **144**, 1669–1694, https://doi.org/10.1175/MWR-D-15-0242.1.

Bjerknes, J., and H. Solberg, 1922: Life cycle of cyclones and the polar front theory of atmospheric circulation. *Geofys. Publ.*, **3**, 3–18, https://doi.org/10.1002/QJ.49704920609.

Blaylock, B. K., and J. D. Horel, 2015: Archive of the High-Resolution Rapid Refresh model (updated in real time). University of Utah, accessed 10 October 2018, https://doi.org/10.7278/S5JQ0Z5B.

——, ——, and S. T. Liston, 2017: Cloud archiving and data mining of High-Resolution Rapid Refresh forecast model output. *Comput. Geosci.*, **109**, 43–50, https://doi.org/10.1016/j.cageo.2017.08.005.

BOM, 2019: Madden-Julian Oscillation data archive. Bureau of Meteorology–Australian government, accessed 15 April 2019, http://www.bom.gov.au/climate/mjo/graphics/rmm.74toRealtime.txt.

Browning, K. A., 1986: Conceptual models of precipitation systems. *Wea. Forecasting*, **1**, 23–41, https://doi.org/10.1175/1520-0434(1986)001<0023:CMOPS>2.0.CO;2.

——, and C. W. Pardoe, 1973: Structure of low-level jet streams ahead of mid-latitude cold fronts. *Quart. J. Roy. Meteor. Soc.*, **99**, 619–638, https://doi.org/10.1002/qj.49709942204.

CADWR, 2019: Hourly precipitation data. California Department of Water Resources–California Data Exchange Center, accessed 15 November 2019, https://cdec.water.ca.gov/.

Carlson, T. N., 1980: Airflow through midlatitude cyclones and the comma cloud pattern. *Mon. Wea. Rev.*, **108**, 1498–1509, https://doi.org/10.1175/1520-0493(1980)108<1498:ATMCAT>2.0.CO;2.

Carrera, M. L., R. W. Higgins, and V. E. Kousky, 2004: Downstream weather impacts associated with atmospheric blocking over the Northeast Pacific. *J. Climate*, **17**, 4823–4839, https://doi.org/10.1175/JCLI-3237.1.

Chang, E. K. M., S. Lee, and K. L. Swanson, 2002: Storm track dynamics. *J. Climate*, **15**, 2163–2183, https://doi.org/10.1175/1520-0442(2002)015<02163:STD>2.0.CO;2.

Colucci, S. J., 1985: Explosive cyclogenesis and large-scale circulation changes: Implications for atmospheric blocking. *J. Atmos. Sci.*, **42**, 2701–2717, https://doi.org/10.1175/1520-0469(1985)042<2701:ECALSC>2.0.CO;2.

Cordeira, J. M., F. Martin Ralph, and B. J. Moore, 2013: The development and evolution of two atmospheric rivers in proximity to western North Pacific tropical cyclones in October 2010. *Mon. Wea. Rev.*, **141**, 4234–4255, https://doi.org/10.1175/MWR-D-13-00019.1.

Croci-Maspoli, M., C. Schwierz, and H. C. Davies, 2007: Atmospheric blocking: Space-time links to the NAO and PNA. *Climate Dyn.*, **29**, 713–725, https://doi.org/10.1007/s00382-007-0259-4.

Dee, D. P., and Coauthors, 2011: The ERA-Interim reanalysis: Configuration and performance of the data assimilation system. *Quart. J. Roy. Meteor. Soc.*, **137**, 553–597, https://doi.org/10.1002/qj.828.

Dettinger, M. D., F. M. Ralph, T. Das, P. J. Neiman, and D. R. Cayan, 2011: Atmospheric rivers, floods and the water resources of California. *Water*, **3**, 445–478, https://doi.org/10.3390/w3020445.

Dole, R. M., and R. X. Black, 1990: Life cycles of persistent anomalies. Part II: The development of persistent negative height anomalies over the North Pacific Ocean. *Mon. Wea. Rev.*, **118**, 824–846, https://doi.org/10.1175/1520-0493(1990)118<0824:LCOPAP>2.0.CO;2.

Dong, L., L. R. Leung, F. Song, and J. Lu, 2018: Roles of SST versus internal atmospheric variability in winter extreme precipitation variability along the U.S. West Coast. *J. Climate*, **31**, 8039–8058, https://doi.org/10.1175/JCLI-D-18-0062.1.

Doswell, C. A., H. E. Brooks, and R. A. Maddox, 1996: Flash flood forecasting: An ingredients-based methodology. *Wea. Forecasting*, **11**, 560–581, https://doi.org/10.1175/1520-0434(1996)011<0560:FFFAIB>2.0.CO;2.

Eady, E. T., 1949: Long waves and cyclone waves. *Tellus*, **1**, 33–52, https://doi.org/10.3402/tellusa.v1i3.8507.

ECMWF, 2009: ERA-Interim Project (updated monthly). NCAR Computational and Information Systems Laboratory Research Data Archive, accessed 27 March 2018, https://doi.org/10.5065/D6CR5RD9.

Fish, M. A., A. M. Wilson, and F. M. Ralph, 2019: Atmospheric river families: Definition and associated synoptic conditions. *J. Hydrometeor.*, **20**, 2091–2108, https://doi.org/10.1175/JHM-D-18-0217.1.

Grams, C. M., and H. M. Archambault, 2016: The key role of diabatic outflow in amplifying the midlatitude flow: A representative case study of weather systems surrounding western North Pacific extratropical transition. *Mon. Wea. Rev.*, **144**, 3847–3869, https://doi.org/10.1175/MWR-D-15-0419.1.

——, H. Binder, S. Pfahl, N. Piaget, and H. Wernli, 2014: Atmospheric processes triggering the central European floods in June 2013. *Nat. Hazards Earth Syst. Sci.*, **14**, 1691–1702, https://doi.org/10.5194/nhess-14-1691-2014.

Harrold, T. W., 1973: Mechanisms influencing the distribution of precipitation within baroclinic disturbances. *Quart. J. Roy. Meteor. Soc.*, **99**, 232–251, https://doi.org/10.1002/qj.49709942003.

Hatchett, B. J., B. Daudert, C. B. Garner, N. S. Oakley, A. E. Putnam, and A. B. White, 2017: Winter snow level rise in the northern Sierra Nevada from 2008 to 2017. *Water*, **9**, 899, https://doi.org/10.3390/w9110899.

Hecht, C. W., and J. M. Cordeira, 2017: Characterizing the influence of atmospheric river orientation and intensity on precipitation distributions over North Coastal California. *Geophys. Res. Lett.*, **44**, 9048–9058, https://doi.org/10.1002/2017GL074179.

Higgins, R. W., and K. C. Mo, 1997: Persistent North Pacific circulation anomalies and the tropical intraseasonal oscillation. *J. Climate*, **10**, 223–244, https://doi.org/10.1175/1520-0442(1997)010<0223:PNPCAA>2.0.CO;2.

——, J.-K. E. Schemm, W. Shi, and A. Leetmaa, 2000a: Extreme precipitation events in the western United States related to tropical forcing. *J. Climate*, **13**, 793–820, https://doi.org/10.1175/1520-0442(2000)013<0793:EPEITW>2.0.CO;2.

——, W. Shi, E. Yarosh, and R. Joyce, 2000b: Improved United States precipitation quality control system and analysis. NCEP/Climate Prediction Center Atlas 7, NOAA, 40 pp., http://www.cpc.ncep.noaa.gov/research_papers/ncep_cpc_atlas/7/toc.html.

Hoskins, B. J., I. Draghici, and H. C. Davies, 1978: A new look at the $\omega$-equation. *Quart. J. Roy. Meteor. Soc.*, **104**, 31–38, https://doi.org/10.1002/qj.49710443903.

Hu, H., F. Dominguez, Z. Wang, D. A. Lavers, G. Zhang, and F. M. Ralph, 2017: Linking atmospheric river hydrological impacts on the U.S. West Coast to Rossby wave breaking. *J. Climate*, **30**, 3381–3399, https://doi.org/10.1175/JCLI-D-16-0386.1.

Junker, N. W., R. H. Grumm, R. Hart, L. F. Bosart, K. M. Bell, and F. J. Pereira, 2008: Use of normalized anomaly fields to anticipate extreme rainfall in the mountains of Northern California. *Wea. Forecasting*, **23**, 336–356, https://doi.org/10.1175/2007WAF2007013.1.

Knutson, T. R., and K. M. Weickmann, 1987: 30–60 day atmospheric oscillations: Composite life cycles of convection and circulation anomalies. *Mon. Wea. Rev.*, **115**, 1407–1436, https://doi.org/10.1175/1520-0493(1987)115<1407:DAOCLC>2.0.CO;2.

Lenggenhager, S., and O. Martius, 2019: Atmospheric blocks modulate the odds of heavy precipitation events in Europe. *Climate Dyn.*, **53**, 4155–4171, https://doi.org/10.1007/s00382-019-04779-0.

——, M. Croci-Maspoli, S. Brönnimann, and O. Martius, 2019: On the dynamical coupling between atmospheric blocks and heavy precipitation events: A discussion of the southern Alpine flood in October 2000. *Quart. J. Roy. Meteor. Soc.*, **145**, 530–545, https://doi.org/10.1002/QJ.3449.

Liebmann, B., and C. A. Smith, 1996: Description of a complete (interpolated) outgoing longwave radiation dataset. *Bull. Amer. Meteor. Soc.*, **77**, 1275–1277.

Lin, Y., 2011: NCEP 4-km Gridded Stage IV Data, Version 1.0. UCAR/NCAR Earth Observing Laboratory Archive, accessed 20 October 2018, https://doi.org/10.5065/D6PG1QDD.

Lindzen, R. S., and B. Farrell, 1980: A simple approximate result for the maximum growth rate of baroclinic instabilities. *J. Atmos. Sci.*, **37**, 1648–1654, https://doi.org/10.1175/1520-0469(1980)037<1648:ASARFT>2.0.CO;2.

Maddox, R. A., F. Canova, and L. R. Hoxit, 1980: Meteorological characteristics of flash flood events over the western United States. *Mon. Wea. Rev.*, **108**, 1866–1877, https://doi.org/10.1175/1520-0493(1980)108<1866:MCOFFE>2.0.CO;2.

Madonna, E., H. Wernli, H. Joos, and O. Martius, 2014: Warm conveyor belts in the ERA-Interim dataset (1979–2010). Part I: Climatology and potential vorticity evolution. *J. Climate*, **27**, 3–26, https://doi.org/10.1175/JCLI-D-12-00720.1.

Martin, J. E., 2006: The role of shearwise and transverse quasi-geostrophic vertical motions in the midlatitude cyclone life cycle. *Mon. Wea. Rev.*, **134**, 1174–1193, https://doi.org/10.1175/MWR3114.1.

Martius, O., C. Schwierz, and H. C. Davies, 2007: Breaking waves at the tropopause in the wintertime Northern Hemisphere: Climatological analyses of the orientation and the theoretical LC1/2 classification. *J. Atmos. Sci.*, **64**, 2576–2592, https://doi.org/10.1175/JAS3977.1.

——, ——, and ——, 2010: Tropopause-level waveguides. *J. Atmos. Sci.*, **67**, 866–879, https://doi.org/10.1175/2009JAS2995.1.

——, and Coauthors, 2013: The role of upper-level dynamics and surface processes for the Pakistan flood of July 2010. *Quart. J. Roy. Meteor. Soc.*, **139**, 1780–1797, https://doi.org/10.1002/qj.2082.

McIntyre, M. E., and T. N. Palmer, 1983: Breaking planetary waves in the stratosphere. *Nature*, **305**, 593–600, https://doi.org/10.1038/305593a0.

——, and ——, 1984: The ''surf zone'' in the stratosphere. *J. Atmos. Terr. Phys.*, **46**, 825–849, https://doi.org/10.1016/0021-9169(84)90063-1.

Mo, K. C., and R. W. Higgins, 1998: Tropical influences on California precipitation. *J. Climate*, **11**, 412–430, https://doi.org/10.1175/1520-0442(1998)011<0412:TIOCP>2.0.CO;2.

Moore, B. J., D. Keyser, and L. F. Bosart, 2019: Linkages between extreme precipitation events in the central and eastern U.S. and Rossby wave breaking. *Mon. Wea. Rev.*, **147**, 3327–3349, https://doi.org/10.1175/MWR-D-19-0047.1.

Moore, R. W., O. Martius, T. Spengler, R. W. Moore, O. Martius, and T. Spengler, 2010: The modulation of the subtropical and extratropical atmosphere in the Pacific basin in response to the Madden-Julian Oscillation. *Mon. Wea. Rev.*, **138**, 2761–2779, https://doi.org/10.1175/2010MWR3194.1.

Mullen, S. L., 1987: Transient eddy forcing of blocking flows. *J. Atmos. Sci.*, **44**, 3–22, https://doi.org/10.1175/1520-0469(1987)044<0003:TEFOBF>2.0.CO;2.

Nakamura, H., and J. M. Wallace, 1990: Observed changes in baroclinic wave activity during the life cycles of low-frequency circulation anomalies. *J. Atmos. Sci.*, **47**, 1100–1116, https://doi.org/10.1175/1520-0469(1990)047<1100:OCIBWA>2.0.CO;2.

——, and ——, 1993: Synoptic behavior of baroclinic eddies during the blocking onset. *Mon. Wea. Rev.*, **121**, 1892–1903, https://doi.org/10.1175/1520-0493(1993)121<1892:SBOBED>2.0.CO;2.

Neiman, P. J., F. M. Ralph, A. B. White, D. E. Kingsmill, and P. O. G. Persson, 2002: The statistical relationship between upslope flow and rainfall in California's coastal mountains: Observations during CALJET. *Mon. Wea. Rev.*, **130**, 1468–1492, https://doi.org/10.1175/1520-0493(2002)130<1468:TSRBUF>2.0.CO;2.

——, ——, G. A. Wick, J. D. Lundquist, and M. D. Dettinger, 2008: Meteorological characteristics and overland precipitation impacts of atmospheric rivers affecting the West Coast of North America based on eight years of SSM/I satellite observations. *J. Hydrometeor.*, **9**, 22–47, https://doi.org/10.1175/2007JHM855.1.

——, B. J. Moore, A. B. White, G. A. Wick, J. Aikins, D. L. Jackson, J. R. Spackman, and F. M. Ralph, 2016: An airborne and ground-based study of a long-lived and intense atmospheric river with mesoscale frontal waves impacting California during CalWater-2014. *Mon. Wea. Rev.*, **144**, 1115–1144, https://doi.org/10.1175/MWR-D-15-0319.1.

Newell, R. E., N. E. Newell, Y. Zhu, and C. Scott, 1992: Tropospheric rivers?—A pilot study. *Geophys. Res. Lett.*, **19**, 2401–2404, https://doi.org/10.1029/92GL02916.

NOAA/NCEI, 2018: 2017 National Climate Report. NOAA/National Centers for Environmental Information, accessed 15 September 2018, https://www.ncdc.noaa.gov/sotc/national/201713.

NOAA/NCEP/CPC, 2018: Daily U.S. Unified Precipitation Dataset (updated daily). NOAA/OAR/ESRL/PSD Gridded Climate Dataset Archive, accessed 15 January 2018, https://www.esrl.noaa.gov/psd/data/gridded/data.unified.html.

NOAA/NWS/CNRFC, 2018: Heavy precipitation events in California and Northern Nevada during January and February 2017. NOAA/National Weather Service/California–Nevada River Forecast Center, accessed 15 September 2018, https://www.cnrfc.noaa.gov/storm_summaries/janfeb2017storms.php.

NOAA/OAR/ESRL/PSD, 2018: Wind profiler and GPS integrated water vapor data (updated in real time). NOAA/OAR/ESRL/PSD Data and Image Library, accessed 15 November 2018, https://www.esrl.noaa.gov/psd/data/obs/datadisplay/.

——, 2019a: Multivariate ENSO index version 2. NOAA/OAR/ESRL/PSD ENSO Information Page, accessed 5 February 2019, https://www.esrl.noaa.gov/psd/enso/.

——, 2019b: NOAA interpolated outgoing longwave radiation data. NOAA/OAR/ESRL/PSD Gridded Climate Dataset Archive, accessed 5 February 2019, https://www.esrl.noaa.gov/psd/data/gridded/data.interp_OLR.html.

Orlanski, I., and J. Sheldon, 1993: A case of downstream baroclinic development over western North America. *Mon. Wea. Rev.*, **121**, 2929–2950, https://doi.org/10.1175/1520-0493(1993)121<2929:ACODBD>2.0.CO;2.

Payne, A. E., and G. Magnusdottir, 2014: Dynamics of landfalling atmospheric rivers over the North Pacific in 30 years of MERRA reanalysis. *J. Climate*, **27**, 7133–7150, https://doi.org/10.1175/JCLI-D-14-00034.1.

——, and ——, 2016: Persistent landfalling atmospheric rivers over the west coast of North America. *J. Geophys. Res. Atmos.*, **121**, 13 287–13 300, https://doi.org/10.1002/2016JD025549.

Pfahl, S., and H. Wernli, 2012: Quantifying the relevance of cyclones for precipitation extremes. *J. Climate*, **25**, 6770–6780, https://doi.org/10.1175/JCLI-D-11-00705.1.

——, E. Madonna, M. Boettcher, H. Joos, and H. Wernli, 2014: Warm conveyor belts in the ERA-Interim dataset (1979–2010). Part II: Moisture origin and relevance for precipitation. *J. Climate*, **27**, 27–40, https://doi.org/10.1175/JCLI-D-13-00223.1.

——, C. Schwierz, M. Croci-Maspoli, C. M. Grams, and H. Wernli, 2015: Importance of latent heat release in ascending air streams for atmospheric blocking. *Nat. Geosci.*, **8**, 610–614, https://doi.org/10.1038/ngeo2487.

Pinto, J. G., I. Gómara, G. Masato, H. F. Dacre, T. Woollings, and R. Caballero, 2014: Large-scale dynamics associated with clustering of extratropical cyclones affecting Western Europe. *J. Geophys. Res. Atmos.*, **119**, 13 704–13 719, https://doi.org/10.1002/2014JD022305.

Press, W. H., S. A. Teukolsky, W. T. Vetterling, and B. P. Flannery, 2007: *Numerical Recipes: The Art of Scientific Computing*. 3rd ed. Cambridge University Press, 1235 pp.

Priestley, M. D. K., J. G. Pinto, H. F. Dacre, and L. C. Shaffrey, 2017a: Rossby wave breaking, the upper level jet, and serial clustering of extratropical cyclones in western Europe. *Geophys. Res. Lett.*, **44**, 514–521, https://doi.org/10.1002/2016GL071277.

——, ——, ——, and ——, 2017b: The role of cyclone clustering during the stormy winter of 2013/2014. *Weather*, **72**, 187–192, https://doi.org/10.1002/wea.3025.

Ralph, F. M., and M. D. Dettinger, 2012: Historical and national perspectives on extreme West Coast precipitation associated with atmospheric rivers during December 2010. *Bull. Amer. Meteor. Soc.*, **93**, 783–790, https://doi.org/10.1175/BAMS-D-11-00188.1.

——, P. J. Neiman, and G. A. Wick, 2004: Satellite and CALJET aircraft observations of atmospheric rivers over the eastern North Pacific Ocean during the winter of 1997/98. *Mon. Wea. Rev.*, **132**, 1721–1745, https://doi.org/10.1175/1520-0493(2004)132<1721:SACAOO>2.0.CO;2.

——, ——, ——, and R. Rotunno, 2005: Dropsonde observations in low-level jets over the northeastern Pacific Ocean from CALJET-1998 and PACJET-2001: Mean vertical-profile and atmospheric river characteristics. *Mon. Wea. Rev.*, **133**, 889–910, https://doi.org/10.1175/MWR2896.1.

——, ——, ——, S. I. Gutman, M. D. Dettinger, D. R. Cayan, and A. B. White, 2006: Flooding on California's Russian river: Role of atmospheric rivers. *Geophys. Res. Lett.*, **33**, L13801, https://doi.org/10.1029/2006GL026689.

——, ——, G. N. Kiladis, K. Weickmann, and D. W. Reynolds, 2011: A multiscale observational case study of a Pacific atmospheric river exhibiting tropical–extratropical connections and a mesoscale frontal wave. *Mon. Wea. Rev.*, **139**, 1169–1189, https://doi.org/10.1175/2010MWR3596.1.

——, T. Coleman, P. J. Neiman, R. J. Zamora, and M. D. Dettinger, 2013: Observed impacts of duration and seasonality of atmospheric river landfalls on soil moisture and runoff in coastal northern California. *J. Hydrometeor.*, **14**, 443–459, https://doi.org/10.1175/JHM-D-12-076.1.

——, M. D. Dettinger, M. M. Cairns, T. J. Galarneau, and J. Eylander, 2018: Defining ''atmospheric river'': How the glossary of meteorology helped resolve a debate. *Bull. Amer. Meteor. Soc.*, **99**, 837–839, https://doi.org/10.1175/BAMS-D-17-0157.1.

Rasmusson, E. M., and K. Mo, 1993: Linkages between 200-mb tropical and extratropical circulation anomalies during the 1986–1989 ENSO cycle. *J. Climate*, **6**, 595–616, https://doi.org/10.1175/1520-0442(1993)006<0595:LBMTAE>2.0.CO;2.

Renwick, J. A., and J. M. Wallace, 1996: Relationships between North Pacific wintertime blocking, El Niño, and the PNA pattern. *Mon. Wea. Rev.*, **124**, 2071–2076, https://doi.org/10.1175/1520-0493(1996)124<2071:RBNPWB>2.0.CO;2.

Röthlisberger, M., O. Martius, and H. Wernli, 2018: Northern Hemisphere Rossby wave initiation events on the extratropical jet—A climatological analysis. *J. Climate*, **31**, 743–760, https://doi.org/10.1175/JCLI-D-17-0346.1.

Rutz, J. J., W. J. Steenburgh, and F. M. Ralph, 2014: Climatological characteristics of atmospheric rivers and their inland penetration over the western United States. *Mon. Wea. Rev.*, **142**, 905–921, https://doi.org/10.1175/MWR-D-13-00168.1.

Ryoo, J.-M., Y. Kaspi, D. W. Waugh, G. N. Kiladis, D. E. Waliser, E. J. Fetzer, and J. Kim, 2013: Impact of Rossby wave breaking on U.S. West Coast winter precipitation during ENSO events. *J. Climate*, **26**, 6360–6382, https://doi.org/10.1175/JCLI-D-12-00297.1.

Sardeshmukh, P. D., and B. J. Hoskins, 1988: The generation of global rotational flow by steady idealized tropical divergence. *J. Atmos. Sci.*, **45**, 1228–1251, https://doi.org/10.1175/1520-0469(1988)045<1228:TGOGRF>2.0.CO;2.

Scherrer, S. C., M. Croci-Maspoli, C. Schwierz, and C. Appenzeller, 2006: Two-dimensional indices of atmospheric blocking and their statistical relationship with winter climate patterns in the Euro-Atlantic region. *Int. J. Climatol.*, **26**, 233–249, https://doi.org/10.1002/joc.1250.

Schwierz, C., M. Croci-Maspoli, and H. C. Davies, 2004: Perspicacious indicators of atmospheric blocking. *Geophys. Res. Lett.*, **31**, L06125, https://doi.org/10.1029/2003GL019341.

Shapiro, M. A., and Coauthors, 1999: A planetary-scale to mesoscale perspective on the life cycles of extratropical cyclones: The bridge between theory and observations. *The Life Cycles of Extratropical Cyclones*, M. A. Shapiro and S. Grønås, Eds., Amer. Meteor. Soc., 139–185.

——, H. Wernli, N. A. Bond, and R. Langland, 2001: The influence of the 1997–99 El Niño–Southern Oscillation on extratropical baroclinic life cycles over the eastern North Pacific. *Quart. J. Roy. Meteor. Soc.*, **127**, 331–342, https://doi.org/10.1002/QJ.49712757205.

Shutts, G. J., 1983: The propagation of eddies in diffluent jetstreams: Eddy vorticity forcing of 'blocking' flow fields. *Quart. J. Roy. Meteor. Soc.*, **109**, 737–761, https://doi.org/10.1002/QJ.49710946204.

Simmons, A. J., and B. J. Hoskins, 1979: The downstream and upstream development of unstable baroclinic waves. *J. Atmos. Sci.*, **36**, 1239–1254, https://doi.org/10.1175/1520-0469(1979)036<1239:TDAUDO>2.0.CO;2.

Smith, B. L., S. E. Yuter, P. J. Neiman, and D. E. Kingsmill, 2010: Water vapor fluxes and orographic precipitation over northern California associated with a landfalling atmospheric river. *Mon. Wea. Rev.*, **138**, 74–100, https://doi.org/10.1175/2009MWR2939.1.

Sodemann, H., and A. Stohl, 2013: Moisture origin and meridional transport in atmospheric rivers and their association

with multiple cyclones. *Mon. Wea. Rev.*, **141**, 2850–2868, https://doi.org/10.1175/MWR-D-12-00256.1.

Spensberger, C., and T. Spengler, 2014: A new look at deformation as a diagnostic for large-scale flow. *J. Atmos. Sci.*, **71**, 4221–4234, https://doi.org/10.1175/JAS-D-14-0108.1.

Sprenger, M., and Coauthors, 2017: Global climatologies of Eulerian and Lagrangian flow features based on ERA-Interim. *Bull. Amer. Meteor. Soc.*, **98**, 1739–1748, https://doi.org/10.1175/BAMS-D-15-00299.1.

Takaya, K., and H. Nakamura, 2001: A formulation of a phase-independent wave-activity flux for stationary and migratory quasigeostrophic eddies on a zonally varying basic flow. *J. Atmos. Sci.*, **58**, 608–627, https://doi.org/10.1175/1520-0469(2001)058<0608:AFOAPI>2.0.CO;2.

Thorncroft, C. D., B. J. Hoskins, and M. E. Mcintyre, 1993: Two paradigms of baroclinic-wave life-cycle behaviour. *Quart. J. Roy. Meteor. Soc.*, **119**, 17–55, https://doi.org/10.1002/qj.49711950903.

UCAR/NCAR/CISL/TDD, 2018: The NCAR Command Language, version 6.5.0. NCAR, accessed 1 August 2018, http://doi.org/10.5065/D6WD3XH5.

Underwood, S. J., M. L. Kaplan, and K. C. King, 2009: The role of upstream midtropospheric circulations in the Sierra Nevada enabling leeside (spillover) precipitation. Part I: A synoptic-scale analysis of spillover precipitation and flooding in a lee-side basin. *J. Hydrometeor.*, **10**, 1309–1326, https://doi.org/10.1175/2009JHM1105.1.

Wang, S.-Y. S., J.-H. Yoon, E. Becker, and R. Gillies, 2017: California from drought to deluge. *Nat. Climate Change*, **7**, 465–468, https://doi.org/10.1038/nclimate3330.

Weaver, R. L., 1962: Meteorology of hydrologically critical storms in California. U.S. Weather Bureau Hydrometeorological Rep. 37, 227 pp., http://www.nws.noaa.gov/oh/hdsc/PMP_documents/HMR37.pdf.

Wernli, H., 1997: A Lagrangian-based analysis of extratropical cyclones. II: A detailed case-study. *Quart. J. Roy. Meteor. Soc.*, **123**, 1677–1706, https://doi.org/10.1002/qj.49712354211.

——, and C. Schwierz, 2006: Surface cyclones in the ERA-40 dataset (1958–2001). Part I: Novel identification method and global climatology. *J. Atmos. Sci.*, **63**, 2486–2507, https://doi.org/10.1175/JAS3766.1.

——, and M. Sprenger, 2007: Identification and ERA-15 climatology of potential vorticity streamers and cutoffs near the extratropical tropopause. *J. Atmos. Sci.*, **64**, 1569–1586, https://doi.org/10.1175/JAS3912.1.

——, S. Pfahl, J. Trentmann, and M. Zimmer, 2010: How representative were the meteorological conditions during the COPS field experiment in summer 2007? *Meteor. Z.*, **19**, 619–630, https://doi.org/10.1127/0941-2948/2010/0483.

Wheeler, M., and K. M. Weickmann, 2001: Real-time monitoring and prediction of modes of coherent synoptic to intraseasonal tropical variability. *Mon. Wea. Rev.*, **129**, 2677–2694, https://doi.org/10.1175/1520-0493(2001)129<2677:RTMAPO>2.0.CO;2.

——, and H. H. Hendon, 2004: An all-season real-time multivariate MJO index: Development of an index for monitoring and prediction. *Mon. Wea. Rev.*, **132**, 1917–1932, https://doi.org/10.1175/1520-0493(2004)132<1917:AARMMI>2.0.CO;2.

White, A. B., P. J. Neiman, J. M. Creamean, T. Coleman, F. M. Ralph, and K. A. Prather, 2015: The impacts of California's San Francisco Bay area gap on precipitation observed in the Sierra Nevada during HMT and CalWater. *J. Hydrometeor.*, **16**, 1048–1069, https://doi.org/10.1175/JHM-D-14-0160.1.

——, B. J. Moore, D. J. Gottas, and P. J. Neiman, 2019: Winter storm conditions leading to excessive runoff above California's Oroville Dam during January and February 2017. *Bull. Amer. Meteor. Soc.*, **100**, 55–70, https://doi.org/10.1175/BAMS-D-18-0091.1.

Wilks, D. S., 2011: *Statistical Methods in the Atmospheric Sciences*. 3rd ed. International Geophysics Series, Vol. 100, Academic Press, 704 pp.

Winters, A. C., D. Keyser, and L. F. Bosart, 2019: The development of the North Pacific jet phase diagram as an objective tool to monitor the state and forecast skill of the upper-tropospheric flow pattern. *Wea. Forecasting*, **34**, 199–219, https://doi.org/10.1175/WAF-D-18-0106.1.

Wirth, V., M. Riemer, E. K. M. Chang, and O. Martius, 2018: Rossby wave packets on the midlatitude waveguide—A review. *Mon. Wea. Rev.*, **146**, 1965–2001, https://doi.org/10.1175/MWR-D-16-0483.1.

Wolf, G., and V. Wirth, 2017: Diagnosing the horizontal propagation of Rossby wave packets along the midlatitude waveguide. *Mon. Wea. Rev.*, **145**, 3247–3264, https://doi.org/10.1175/MWR-D-16-0355.1.

Wolter, K., and M. S. Timlin, 2011: El Niño/Southern Oscillation behaviour since 1871 as diagnosed in an extended multivariate ENSO index (MEI.ext). *Int. J. Climatol.*, **31**, 1074–1087, https://doi.org/10.1002/joc.2336.

Woollings, T., and Coauthors, 2018: Blocking and its response to climate change. *Curr. Climate Change Rep.*, **4**, 287–300, https://doi.org/10.1007/s40641-018-0108-z.

Zhu, Y., and R. E. Newell, 1998: A proposed algorithm for moisture fluxes from atmospheric rivers. *Mon. Wea. Rev.*, **126**, 725–735, https://doi.org/10.1175/1520-0493(1998)126<0725:APAFMF>2.0.CO;2.